Unambiguous Spacecraft Attitude Determination Using SunMag MEMS Sensor Data

Bachelor's Thesis

Katcha Koch Winther
June 2017

Supervisor:
René Fléron, DTU Space

DTU Space
National Space Institute

Preface

This Bachelor's thesis of 15 ECTS points has been completed at DTU space. The main supervisor of the project was René Fleron. The following pages describe the theoretical, analytical and practical work conducted in the spring and summer of 2017.

Abstract

In this Bachelor's thesis, the usage of the SunMag chip as a means of satellite attitude determination is explored. The attitude determination system of this thesis utilises a solar and a magnetic direction vector to find the Euler angles of the spacecraft. After an examination of the magnetic sensor of the SunMag, the PHEBS, this sensor was deemed inadequate for the attitude determination of this thesis. The sun sensors were however capable of determining the solar body vector for a 360 degree rotation. The attitude determination matrix for a 3-2-1 body axis rotation is derived, and along with the weighted TRIAD algorithm, the attitude of a rotating CubeSat mock-up is determined with a resolution of approximately six degrees.

Contents

1 Introduction

For many spacecraft applications, knowledge of the spacecraft's attitude, i.e. it's orientation or angular position in space, is of great importance to the mission objectives. Often this knowledge is used to correct the attitude of spacecrafts that have direction dependent equipment. Equipment such as cameras observing distant celestial objects or events, or antenna transmitting to or receiving data from Earth based stations.

The basic principle behind attitude determination for any rigid object - spacecraft or not - is to find the angles the axes of a reference frame, F, need to turn in order to align with the axes of the rigid body's coordinate system (the body frame, S). This is done by comparing two or more directional vectors observed from both frames. Two such directional vectors could be the direction to the Sun and the magnetic field vector of the Earth's dipole field at the spacial point of the spacecraft's position at that specific time.

For spacecrafts orbiting the Earth, often the origin of the body frame is set in the spacecrafts centre of mass, and the origin of the reference frame is placed in the centre of the Earth. The most notable Earth centred coordinates systems are the "Earth-centred inertial" (ECI) frame and the "Earth-centred, Earth-fixed" (ECEF) frame. The ECEF frame has its three principal axes intersecting set points on the surface of the Earth - the z-axis goes through geographic north pole, the x-axis goes through 0° latitude and 0° longitude, and the y-axis completes the right-hand coordinate system. The ECEF frame is preferred for orientation and navigation on the surface of the Earth, whereas the ECI frame is preferred for orientation and navigation in the space surrounding the Earth. The ECI frame also has its third principle axis through the geographic north pole, but instead of having its x-axis intersecting a set point on the surface of the Earth, it is placed to intersect a set point in space that does not rotate with respect to the Earth. Often the vernal equinox is used. Again the y-axis completes the right-hand coordinate system.

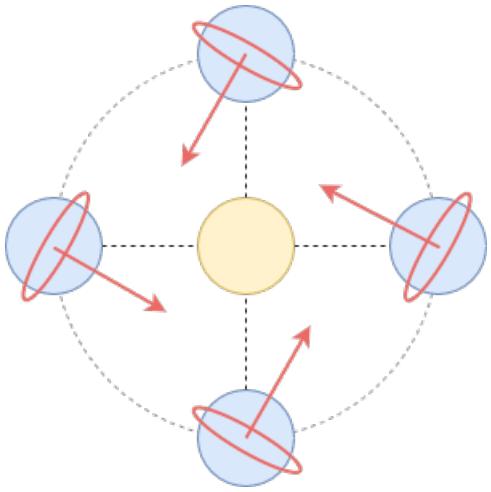

Figure 1: An illustration of the basic principles behind a Sun-synchronous orbit. Here the orbit and its normal is drawn in orange at four different times in the Earth's orbit around the Sun.

Many scientific satellites are in a low-earth-orbit[1] (LEO) [11], and many of these are in a sun-synchronous orbit (SSO). A SSO is defined by having a constant angle between the norm of the orbit and the direction to the Sun, see figure 1. This makes the the directional sun vector, as seen by the Earth-centred reference frame, easy to calculate. As such a SSO is preferable for missions, where the attitude is determined in part through the directional sun vector.

In this thesis, an unambiguous attitude determination system (ADS) using a Sun pointing vector and a magnetic field vector is explored.
The determination of the two directional vectors as seen from the body frame, $\mathbf{b}_1$ and $\mathbf{b}_2$ (here the index 1 refers to the Sun and the index 2 refers to the magnetic field.), will be based on a microelectromechanical system (MEMS) sensor capable of measuring the indent angles of sunlight and the magnetic field vector - the SunMag chip.

The basic layout of the SunMag chip can be seen on figure 2. The two main components of the SunMag chip is a two-axis sun sensor consisting of four photo diodes and a one-axis Planar Hall effect bridge sensor (PHEBS) capable of measuring the magnetic field strength in one direction.

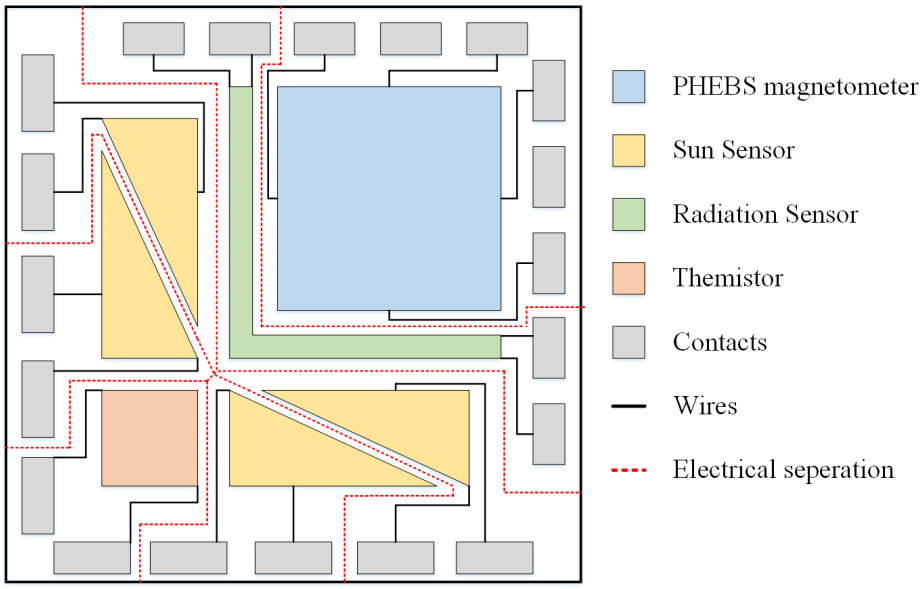

Figure 2: The basic layout of the SunMag chip. Apart from the sun sensors and the PHEBS, it also contains a thermistor and a radiation sensor in the form of a PIN diode. The thermistor is implemented because the sensitivity of the PHEBS is temperature dependent [9], and knowing the temperature should enable computational compensation. The PIN diode does not have any purpose as far as attitude determination goes, but could provide useful insight into the radiation the chip - and as such the satellite - is subjugated to. The thermistor and the PIN diode will not be analysed in this thesis. Source: [1].

[1] Approximately 200 km to 2000 km

The complete fabrication of the SunMag sensor is yet to be completed, but the PHEBS and the sun sensors have been fabricated in separate batches [4], [1], [3]. Thus, testing in this project will be carried out using sun sensors and PHEBS on separate chips.
In the following section an overview of the theory behind the application of the SunMag chip will be explained. For a full explanation of the design, function and fabrication of the SunMag chip, see [9] or [1]. For projects and reports dedicated entirely to either the sun sensor or the PHEBS, see [4] or [8] and [2] respectively.

2 Overview of the Theory and Application of the SunMag Chip

2.1 The Sun Sensor

As can be seen from figure 2 the sun sensor consists of four triangular photo diodes. Each pair can measure the indent angle of the sunlight in either the x- or y-direction, $\theta_{1,x}$ and $\theta_{1,y}$ respectively. Each sun sensor is covered by quartz and a golden layer with a slit placed over the centre of a photo diode pair, see figure 3 (b). Depending on the indent angle of the sunlight the ratio of the illuminated area on the two triangles of a set will vary - and therefore also the ratio of the current the photo diodes produce. This geometry can be seen on figure 3.

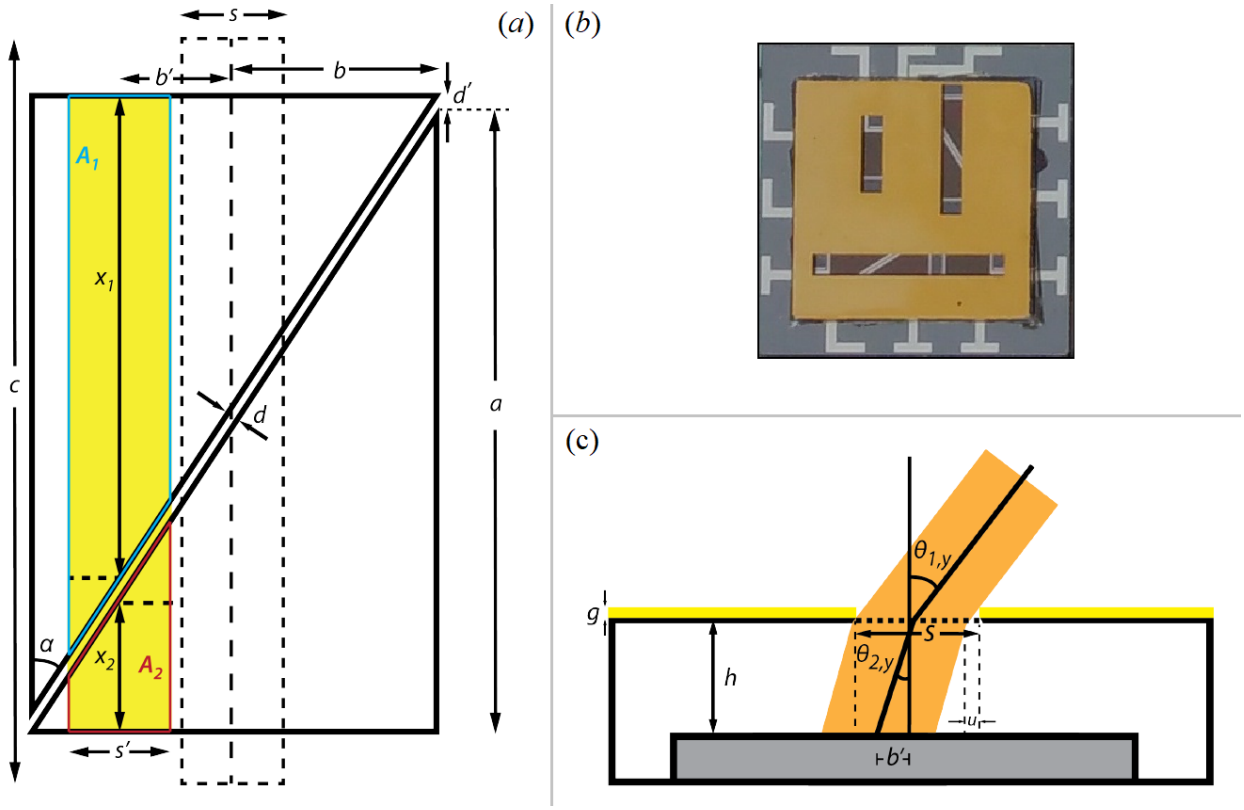

Figure 3: (a) shows a top view of a photo diode and (c) shows a side view of a photo diode. A description of the different dimentions and parameters, as well as their values, can be found in table 1 in appendix A. Source of (a) and (c) is [9]. (b) shows the type of sun sensor chip used for the experimental part of this thesis. Here the majority of the chip is covered by the golden cover. This sensor also has two square reference diodes, but these are not used in this project.

In [9] the geometric dimensions are used to derive a relation between the indent angle of the sunlight, $\theta_{1,y}$ and the current produced by the two triangular photo diodes in a pair, $I_{1,y}$ and $I_{2,y}$

$$\frac{I_{1,y} - I_{2,y}}{I_{1,y} + I_{2,y}} = \frac{2h \tan\left(\arcsin\left(\frac{1}{n_{quartz}} \sin\theta_{1,x}\right) + g \tan\theta_{1,y}\right)}{2b} \tag{1}$$

where $n_{quartz} = 1.458$ is the refraction index of vacuum and quartz, h is the height of the glass cover, g is the thickness of the gold cover and b is the half width of the photo diode.

A similar expression applies to the relation between $I_{1,x}$, $I_{2,x}$ and $\theta_{1,x}$. From here on the indent angles $\theta_{1,x}$ and $\theta_{1,y}$ will simply be referred to as θ_x and θ_y respectively, as equation (1) shows that the currents are independent of $\theta_{2,x}$ and $\theta_{2,y}$. Using equation (1) and the values given in table 1 in appendix A, a graph of the expected current ratios as a function of θ_y as well as its inverse function can be produced, see figure 4.

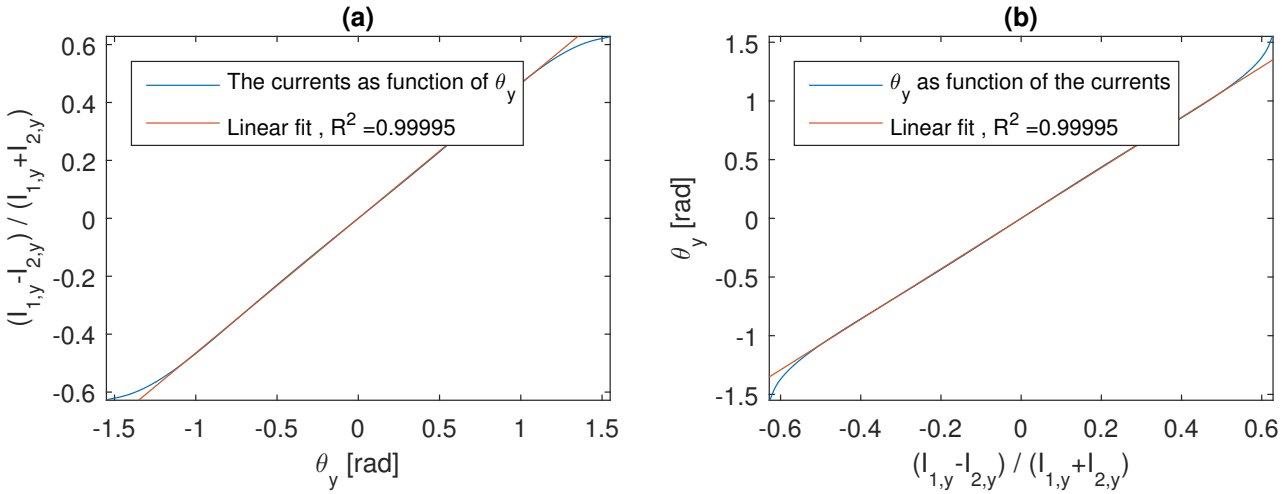

Figure 4: The theoretical relation between the currents generated by the photo diodes and the indent angle

As can be seen on figure 4, the relation is approximately linear in the interval $\theta_y \in$ [-60 deg, 60 deg].
Using a simple linear regression instead of the more complicated expression of equation (1) greatly decreases the computational power needed to calculate the indent angle. This does however make the application of the sunsensors inaccurate in the extreme indent angles. But as will be seen in section 5.1.2 the data generated by the sun sensors for the extreme angles is very unpredictable anyway. Therefore approximating the angle-current relation will not further limit the usable range of the sun sensors.

The sun sensors will be used to calculate the solar direction vector. As the sensor is only usable when light is hitting it, it is safe to assume that the sun vector component parallel with the normal of the surface of the chip (the z_s-component) is positive. Setting the z_s-component to 1, allow the remaining two components to be calculated as

$$\tan\theta_x = \frac{x_s}{z_s} \quad \Rightarrow \quad x_s = z_s \tan\theta_x = \tan\theta_x \tag{2}$$

$$\tan\theta_y = \frac{y_s}{z_s} \quad \Rightarrow \quad y_s = z_s \tan\theta_y = \tan\theta_y \tag{3}$$

In accordance with figure 5. The solar direction vector is then found through normalisation of the components.

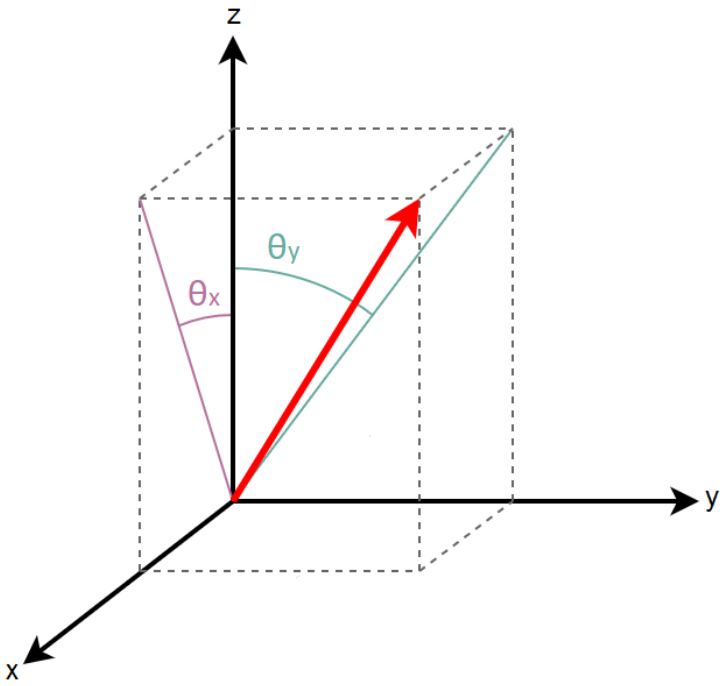

Figure 5: A coordinate system showing the relations between the indent angles θ_x and θ_x. Here the surface of the sun sensor would be parallel with the x, y-plane, and the red vector points towards the light source.

2.2 The PHEBS

The PHEBS ability to measure changes in magnetic fields, comes from the inherent anisotropic magnetoresistance (AMR) effect of ferromagnetic (FM) materials. The AMR effect alters the resistance of the softly magnetised FM material (NiFe) depending on the direction of the outer field. When an outer field is applied the magnetisation of the FM layer will make an angle with the easy axis, resulting in the resistance of the FM layer changing. Applying this property, the PHEBS can determine the magnetic field strength in the direction perpendicular to the easy axis of the sensor, see figure 7. The hardly magnetised antiferromagnetic (AFM) layer (MnIr) forces the magnetisation of the FM layer to be fixed along the easy axis, when no outer field is applied.

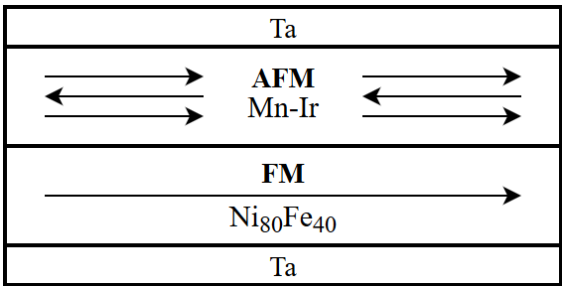

Figure 6: Magnetisation configuration of the magnetic stack metals.

The PHEB magnetic field sensor is designed as a wheatstone bridge as seen in figure 7. The meander structure of the leads, which can be seen on figure 8, allows for long leads on a small surface, increasing the sensitivity and usability of the sensor.

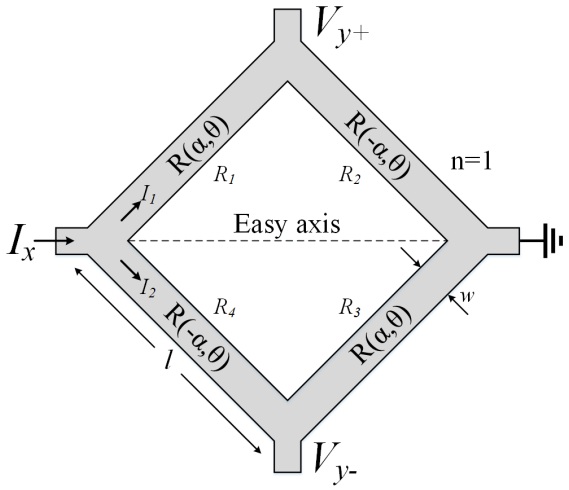

Figure 7: The basic principle behind the PHEBS. Figure slightly edited from [1].

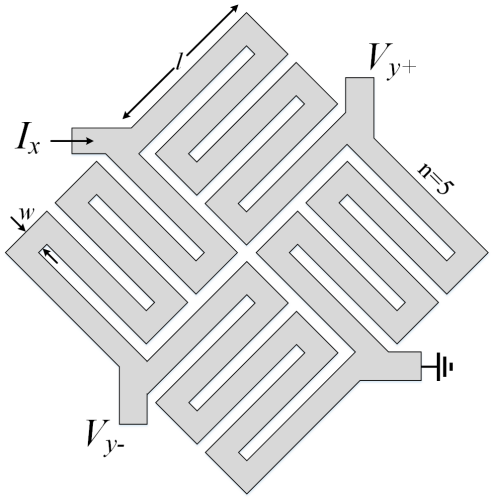

Figure 8: The meander geometry of the PHEBS. For the sensors used in this thesis, $n = 21$. Source: [1].

As the resistance of the meanders change pairwise (either R_1 and R_3 increase while R_2 and R_4 decrease or vice versa), this will offset the bridge voltage $V_y = V_{y+} - V_{y-}$ from zero. How V_y changes as a function of the magnetic field in the y-axis can be seen from equations (4) and (5)[2]. These are derived in [2].

$$V_y = I_x S_0 \mu_0 H_y \qquad (4) \qquad S_0 = \frac{nl\Delta\rho}{wt_{FM}\mu_0 \left(H_{ex} + H_k\right)} \qquad (5)$$

Where;
I_x is the current entering the PHEBS. As the total resistance of the PHEBS, R_{PHEBS}, doesn't change

[2]The expression for V_y given in equation (4) is the low-field signal. The relation between V_y and $\mu_0 H_y$ is only linear in a magnetic interval of less than ± 5 mT. But as the maximum magnetic field strength of the Earth's dipole is within the interval ± 60.000 nT at the surface of the Earth, the magnitude of the magnetic field the PHEBS will be subjucated to in orbit is well within the low-field interval.

regardless of the magnetic field, and as the voltage applied across the bridge, U_{in} is assumed constant[3], I_x is also assumed constant.
S_0 is the normalised sensitivity of the PHEBS given by equation (5).
$\mu_0 H_y = B_y$ is the y-component of the magnetic field.
H_{ex} and H_k are the exchange bias and anisotropy fields respectively, which are found through an hysteresis analysis of the magnetic stack metals [1].
$\Delta\rho = \rho_{||} + \rho_{\perp}$ is the sum of the parallel and perpendicular resistivities of the meander leads.
t_{FM} is the thickness of the ferromagnetic layer.
n is the number of meander leads, l is each lead's length and w its width.

As all elements of equation (5) are constant, and as I_x is assumed constant as well, the bridge voltage, V_y is linearly proportional to the magnetic field in the y-direction, B_y. This means equation (4) can be redefined as

$$V_y = S\mu_0 H_y = SB_y \tag{6}$$

Where S is the specific sensitivity of the PHEBS, and is a function of U_{in} and R_{PHEBS}. S will be determined experimentally during characterisation of the individual PHEBS, as it will vary from sensor to sensor, as the fabrication can result in slightly differing chips[4]. From this point forward, the specific sensitivity will simply be referred to as the sensitivity.
With three orthogonal PHEBS the full magnetic field $\boldsymbol{B} = [\, B_x \;\; B_y \;\; B_z \,]^T$ can be found.

[3] U_{in} is bound to fluctuate slightly.
[4] [3] has shown, that this is indeed the case.

3 Static Attitude Determination

As briefly explained in section 1, the basis of attitude determination is to align the axes of the reference frame, F, with the spacecraft body frame, S. To do this, two direction vectors that can be observed from both frames are needed - here the Sun pointing vector and the magnetic field vector. In the reference frame these two vectors are denoted $\mathbf{r}_1$ and $\mathbf{r}_2$ respectively. In the body frame, they are denoted $\mathbf{b}_1$ and $\mathbf{b}_2$.

The reference vectors are transformed to the body vectors with the attitude determination matrix

$$\mathbf{A}^{S/F}\mathbf{r}_i = \mathbf{b}_i \tag{7}$$

whose elements contain the attitude of the body frame, *S*, as seen from reference frame *F*. To find $\mathbf{A}^{S/F}$ one of Euler's theorems, which states that any rotation is a rotation about a fixed axis, can be utilised. In this section, the general theory and derivation of the direction cosine matrix - the general name for the attitude determination matrix - is explained. Then an algorithm for finding $\mathbf{A}^{S/F}$ from the direction vectors is examined, and finally it is described how the attitude is extracted from $\mathbf{A}^{S/F}$.

3.1 The Direction Cosine Matrix

Given two right hand coordinate frames, *A* and *B*, each comprised of a set of orthogonal 3×1 unit vectors $\mathbf{a}_1, \mathbf{a}_2, \mathbf{a}_3$ and $\mathbf{b}_1, \mathbf{b}_2, \mathbf{b}_3$ respectively, the basis vectors of *B* can be expressed in terms of the basis vectors of *A* as

$$\begin{bmatrix}\mathbf{b}_1^T\\ \mathbf{b}_2^T\\ \mathbf{b}_3^T\end{bmatrix} = \begin{bmatrix}C_{11} & C_{12} & C_{13}\\ C_{21} & C_{22} & C_{23}\\ C_{31} & C_{32} & C_{33}\end{bmatrix}\begin{bmatrix}\mathbf{a}_1^T\\ \mathbf{a}_2^T\\ \mathbf{a}_3^T\end{bmatrix} = \mathbf{C}^{B/A}\begin{bmatrix}\mathbf{a}_1^T\\ \mathbf{a}_2^T\\ \mathbf{a}_3^T\end{bmatrix} \tag{8}$$

where the direction cosine, $C_{ij} \equiv \mathbf{b}_i \cdot \mathbf{a}_j = |\mathbf{b}_i|\,|\mathbf{a}_j| \cos\phi = \cos\phi$ is the cosine of the angle between $\mathbf{b}_i$ and $\mathbf{a}_j$. The entire matrix $\mathbf{C}^{B/A}$, which describes the orientation of *B* relative to *A*, is called the direction cosine matrix.

According to the definition of $\mathbf{C}^{B/A}$, equation (8) can also be expressed as

$$\mathbf{C}^{B/A} = \begin{bmatrix}\mathbf{b}_1\cdot\mathbf{a}_1 & \mathbf{b}_1\cdot\mathbf{a}_2 & \mathbf{b}_1\cdot\mathbf{a}_3\\ \mathbf{b}_2\cdot\mathbf{a}_1 & \mathbf{b}_2\cdot\mathbf{a}_2 & \mathbf{b}_2\cdot\mathbf{a}_3\\ \mathbf{b}_3\cdot\mathbf{a}_1 & \mathbf{b}_3\cdot\mathbf{a}_2 & \mathbf{b}_3\cdot\mathbf{a}_3\end{bmatrix} = \begin{bmatrix}\mathbf{b}_1^T\\ \mathbf{b}_2^T\\ \mathbf{b}_3^T\end{bmatrix}\cdot\begin{bmatrix}\mathbf{a}_1 & \mathbf{a}_2 & \mathbf{a}_3\end{bmatrix} \tag{9}$$

Because each set of basis vectors of *A* and *B* consists of orthogonal unit vectors, the direction cosine matrix is an orthonormal matrix. Therefore the following relation holds true

$$[\mathbf{C}^{B/A}]^{-1} = [\mathbf{C}^{B/A}]^T = \mathbf{C}^{A/B} \tag{10}$$

where $\mathbf{C}^{A/B}$ is the direction cosine matrix describing the orientation of *A* relative to *B*. $\mathbf{C}^{A/B}$ can be expressed - much like $\mathbf{C}^{B/A}$ - as

$$\mathbf{C}^{A/B} = \begin{bmatrix} \mathbf{a}_1 \cdot \mathbf{b}_1 & \mathbf{a}_1 \cdot \mathbf{b}_2 & \mathbf{a}_1 \cdot \mathbf{b}_3 \\ \mathbf{a}_2 \cdot \mathbf{b}_1 & \mathbf{a}_2 \cdot \mathbf{b}_2 & \mathbf{a}_2 \cdot \mathbf{b}_3 \\ \mathbf{a}_3 \cdot \mathbf{b}_1 & \mathbf{a}_3 \cdot \mathbf{b}_2 & \mathbf{a}_3 \cdot \mathbf{b}_3 \end{bmatrix} = \begin{bmatrix} \mathbf{a}_1^T \\ \mathbf{a}_2^T \\ \mathbf{a}_3^T \end{bmatrix} \cdot \begin{bmatrix} \mathbf{b}_1 & \mathbf{b}_2 & \mathbf{b}_3 \end{bmatrix} \tag{11}$$

As $\mathbf{C}^{A/B}$ is also an orthonormal matrix the mirrored relation of (10) is also true;

$$[\mathbf{C}^{A/B}]^{-1} = [\mathbf{C}^{A/B}]^T = \mathbf{C}^{B/A} \tag{12}$$

Given the two frames *A* and *B*, an arbitrary 3×1 vector $\mathbf{h} = [\, h_1 \; h_2 \; h_3 \,]^T$ can be described in terms of the basis vectors in *A* as

$$\mathbf{h} = h_1^A \mathbf{a}_1 + h_2^A \mathbf{a}_2 + h_3^A \mathbf{a}_3 \tag{13}$$

and in terms of the basis vectors in *B* as

$$\mathbf{h} = h_1^B \mathbf{b}_1 + h_2^B \mathbf{b}_2 + h_3^B \mathbf{b}_3 \tag{14}$$

where h_i^A and h_i^B are the *i*th component of $\mathbf{h}$ as seen from *A* and *B* respectively. From equation (14) it is seen, that h_i^B can be written as $h_i^B = \mathbf{b}_i \cdot \mathbf{h}$. Inserting equation (13), the following relations between h_i^A and h_i^B are found

$$h_1^B = \mathbf{b}_1 \cdot \mathbf{h} = \mathbf{b}_1 \cdot (h_1^A \mathbf{a}_1 + h_2^A \mathbf{a}_2 + h_3^A \mathbf{a}_3) = h_1^A (\mathbf{b}_1 \cdot \mathbf{a}_1) + h_2^A (\mathbf{b}_1 \cdot \mathbf{a}_2) + h_3^A (\mathbf{b}_1 \cdot \mathbf{a}_3) \tag{15}$$

$$h_2^B = \mathbf{b}_2 \cdot \mathbf{h} = \mathbf{b}_1 \cdot (h_1^A \mathbf{a}_1 + h_2^A \mathbf{a}_2 + h_3^A \mathbf{a}_3) = h_1^A (\mathbf{b}_2 \cdot \mathbf{a}_1) + h_2^A (\mathbf{b}_2 \cdot \mathbf{a}_2) + h_3^A (\mathbf{b}_2 \cdot \mathbf{a}_3) \tag{16}$$

$$h_3^B = \mathbf{b}_3 \cdot \mathbf{h} = \mathbf{b}_1 \cdot (h_1^A \mathbf{a}_1 + h_2^A \mathbf{a}_2 + h_3^A \mathbf{a}_3) = h_1^A (\mathbf{b}_3 \cdot \mathbf{a}_1) + h_2^A (\mathbf{b}_3 \cdot \mathbf{a}_2) + h_3^A (\mathbf{b}_3 \cdot \mathbf{a}_3) \tag{17}$$

which can be written in matrix form as

$$\begin{bmatrix} h_1^B \\ h_2^B \\ h_3^B \end{bmatrix} = \begin{bmatrix} \mathbf{b}_1 \cdot \mathbf{a}_1 & \mathbf{b}_1 \cdot \mathbf{a}_2 & \mathbf{b}_1 \cdot \mathbf{a}_3 \\ \mathbf{b}_2 \cdot \mathbf{a}_1 & \mathbf{b}_2 \cdot \mathbf{a}_2 & \mathbf{b}_2 \cdot \mathbf{a}_3 \\ \mathbf{b}_3 \cdot \mathbf{a}_1 & \mathbf{b}_3 \cdot \mathbf{a}_2 & \mathbf{b}_3 \cdot \mathbf{a}_3 \end{bmatrix} \begin{bmatrix} h_1^A \\ h_2^A \\ h_3^A \end{bmatrix} = \mathbf{C}^{B/A} \begin{bmatrix} h_1^A \\ h_2^A \\ h_3^A \end{bmatrix} \tag{18}$$

This means, that any vector in *A* can be transformed to frame *B* with the direction cosine matrix, $\mathbf{C}^{B/A}$.

In its essence, the direction cosine matrix, $\mathbf{C}^{B/A}$, describes the three rotations the three principal axes of *A* must make to align with the three principal axes of *B*. This is called body-axis rotation, and can be represented symbolically as

$$\mathbf{C}^{B/A}(\phi_1, \phi_2, \phi_3) : B \leftarrow A \tag{19}$$

Where $\phi_i\,,\ i = 1, 2, 3$ is the Euler angle of rotation i. A body-axis rotation can be either symmetric or asymmetric. A symmetric body-axis rotation could be a 3-1-3 rotation, where first the third principal axis is rotated, then the first and finally the third again. An asymmetric body-axis rotation could be a 3-2-1 rotation, where first the third principal axis is rotated, then the second and finally the first. A total of 12 such body-axis rotations exist[5]. In the following, the direction cosine matrix for a 3-2-1 rotation will be derived, but the procedure is similar for all the body-axis rotations.

For the derivation, the body-axis rotation is divided into three separate rotations, symbolically represented as

$$B \leftarrow A'' \leftarrow A' \leftarrow A \tag{20}$$

Where *A'* is the frame *A* transforms into by rotating the third principal axis of *A*, *A"* is the frame *A'* transforms into by rotating the second principal axis of *A'*, and finally *B* is the frame *A"* transforms into by rotating the first principal axis of *A"*. *A'* and *A"* have the basis vectors $\mathbf{a}'_1$, $\mathbf{a}'_2$, $\mathbf{a}'_3$ and $\mathbf{a}''_1$, $\mathbf{a}''_2$, $\mathbf{a}''_3$ respectively.
The three rotations can be described by the three direction cosine matrices

$$\begin{aligned} \mathbf{C}_3(\phi_3): &\quad A' \leftarrow A \\ \mathbf{C}_2(\phi_2): &\quad A'' \leftarrow A' \\ \mathbf{C}_1(\phi_1): &\quad B \leftarrow A'' \end{aligned} \tag{21}$$

Where the three direction cosine matrices consists of elementary rotations respectively about the third, second, and first axes

$$\mathbf{C}_3(\phi_3) = \begin{bmatrix} \cos\phi_3 & \sin\phi_3 & 0 \\ -\sin\phi_3 & \cos\phi_3 & 0 \\ 0 & 0 & 1 \end{bmatrix} \tag{22}$$

$$\mathbf{C}_2(\phi_2) = \begin{bmatrix} \cos\phi_2 & 0 & -\sin\phi_2 \\ 0 & 1 & 0 \\ \sin\phi_2 & 0 & \cos\phi_1 \end{bmatrix} \tag{23}$$

$$\mathbf{C}_1(\phi_1) = \begin{bmatrix} 1 & 0 & 0 \\ 0 & \cos\phi_1 & \sin\phi_1 \\ 0 & -\sin\phi_1 & \cos\phi_1 \end{bmatrix} \tag{24}$$

Given the definitions of *A*, *A'*, *A"* and *B*, each of the three rotations of equation (21) can be described using equations (22) through (24) as

[5] Symmetric: 1-2-1, 1-3-1, 2-1-2, 2-3-2, 3-1-3, 3-2-3. Asymmetric: 1-2-3, 1-3-2, 2-1-3, 2-3-1, 3-2-1, 3-1-2

$$\begin{bmatrix}\mathbf{a}_1'\\ \mathbf{a}_2'\\ \mathbf{a}_3'\end{bmatrix} = \mathbf{C}_3(\phi_3)\begin{bmatrix}\mathbf{a}_1\\ \mathbf{a}_2\\ \mathbf{a}_3\end{bmatrix} \tag{25}$$

$$\begin{bmatrix}\mathbf{a}_1''\\ \mathbf{a}_2''\\ \mathbf{a}_3''\end{bmatrix} = \mathbf{C}_2(\phi_2)\begin{bmatrix}\mathbf{a}_1'\\ \mathbf{a}_2'\\ \mathbf{a}_3'\end{bmatrix} \tag{26}$$

$$\begin{bmatrix}\mathbf{b}_1\\ \mathbf{b}_2\\ \mathbf{b}_3\end{bmatrix} = \mathbf{C}_1(\phi_1)\begin{bmatrix}\mathbf{a}_1''\\ \mathbf{a}_2''\\ \mathbf{a}_3''\end{bmatrix} \tag{27}$$

The preceding sequence of rotations can then be combined

$$\begin{bmatrix}\mathbf{b}_1\\ \mathbf{b}_2\\ \mathbf{b}_3\end{bmatrix} = \mathbf{C}_1(\phi_1)\begin{bmatrix}\mathbf{a}_1''\\ \mathbf{a}_2''\\ \mathbf{a}_3''\end{bmatrix} = \mathbf{C}_1(\phi_1)\mathbf{C}_2(\phi_2)\begin{bmatrix}\mathbf{a}_1'\\ \mathbf{a}_2'\\ \mathbf{a}_3'\end{bmatrix} = \mathbf{C}_1(\phi_1)\mathbf{C}_2(\phi_2)\mathbf{C}_3(\phi_3)\begin{bmatrix}\mathbf{a}_1\\ \mathbf{a}_2\\ \mathbf{a}_3\end{bmatrix} \tag{28}$$

Now, having arrived at a matrix enabling transformation directly from *A* to to *B* this matrix must be equal to the direction cosine matrix, $\mathbf{C}^{B/A}$

$$\mathbf{C}^{B/A} = \mathbf{C}_1(\phi_1)\mathbf{C}_2(\phi_2)\mathbf{C}_3(\phi_3)$$

$$= \begin{bmatrix} \cos\phi_2\cos\phi_3 & \cos\phi_2\sin\phi_3 & -\sin\phi_2 \\ \sin\phi_1\sin\phi_2\cos\phi_3 - \cos\phi_1\sin\phi_3 & \sin\phi_1\sin\phi_2\sin\phi_3 + \cos\phi_1\cos\phi_3 & \sin\phi_1\cos\phi_2 \\ \cos\phi_1\sin\phi_2\cos\phi_3 + \sin\phi_1\sin\phi_3 & \cos\phi_1\sin\phi_2\sin\phi_3 - \sin\phi_1\cos\phi_3 & \cos\phi_1\cos\phi_2 \end{bmatrix} \tag{29}$$

The attitude determination matrix used in this thesis will be based on an 3-2-1 body axis rotation.

3.2 The TRIAD Algorithm and Wahba's Problem

As it is the orientation of the body frame, S, with respect to the reference frame, F, that is desired, an attitude matrix, $A^{S/F}$ that transforms the two direction vectors from F to S is needed, such as the one described by equation (7). But as the measurements of the body vectors aren't error free, finding a single attitude matrix that transforms both body vectors correctly is impossible.

The basic TRIAD algorithm [6] seeks to avoid this issue by assuming that one of the unit direction vectors are much more accurately defined than the other. This means, that if the measurement of $\mathbf{b}_1$ is more accurate than the measurement of $\mathbf{b}_2$, then the TRIAD algorithm finds an estimate of the attitude matrix, A_{TRIAD}, that satisfies $A_{\text{TRIAD}}\mathbf{r}_1 = \mathbf{b}_1$ exactly, but $A_{\text{TRIAD}}\mathbf{r}_2 = \mathbf{b}_2$ only approximately.

The TRIAD attitude matrix is based on two right-handed orthonormal triads, $\{\mathbf{v}_1\,,\ \mathbf{v}_2\,,\ \mathbf{v}_3\}$ which is placed in the reference frame, and $\{\mathbf{w}_1\,,\ \mathbf{w}_2\,,\ \mathbf{w}_3\}$, which is placed in the spacecraft body frame. Given these two triads, the attitude determination matrix

$$A_{\text{TRIAD}} = \begin{bmatrix} \mathbf{w}_1 & \mathbf{w}_2 & \mathbf{w}_3 \end{bmatrix} \begin{bmatrix} \mathbf{v}_1 & \mathbf{v}_2 & \mathbf{v}_3 \end{bmatrix}^T = \sum_{i=1}^{3} \mathbf{w}_i \mathbf{v}_i^T \tag{30}$$

will transform $\mathbf{v}_i$ into $\mathbf{w}_i$ by $A_{\text{TRIAD}}\mathbf{v}_i = \mathbf{w}_i \ , \quad \text{for } i = 1, 2, 3.$

The two triads are based on the two direction vectors. To ensure, that the two triads are orthonormal, their unit vectors are defined as

$$\mathbf{v}_1 = \mathbf{r}_1 \ , \qquad \mathbf{v}_2 = \mathbf{r}_\times = \frac{\mathbf{r}_1 \times \mathbf{r}_2}{|\mathbf{r}_1 \times \mathbf{r}_2|} \ , \qquad \mathbf{v}_3 = \mathbf{r}_1 \times \mathbf{r}_\times \tag{31}$$

$$\mathbf{w}_1 = \mathbf{b}_1 \ , \qquad \mathbf{w}_2 = \mathbf{b}_\times = \frac{\mathbf{b}_1 \times \mathbf{b}_2}{|\mathbf{b}_1 \times \mathbf{b}_2|} \ , \qquad \mathbf{w}_3 = \mathbf{b}_1 \times \mathbf{b}_\times \tag{32}$$

in accordance with equation (30), the estimate of the attitude matrix is then

$$\hat{A}_{TRIAD}^{S/F} = \mathbf{w}_1\mathbf{v}_1^T + \mathbf{w}_3\mathbf{v}_3^T + \mathbf{w}_2\mathbf{v}_2^T = \mathbf{b}_1\mathbf{r}_1^T + (\mathbf{b}_1 \times \mathbf{b}_\times)(\mathbf{r}_1 \times \mathbf{r}_\times)^T + \mathbf{b}_\times\mathbf{r}_\times^T \tag{33}$$

Of course none of the two body vectors are perfectly defined. Therefore the TRIAD algorithm can be expanded by solving Wahba's problem for two observations.

In attitude determination, Wahba's problem[6] consists of finding an orthogonal matrix A with determinant +1 that minimizes the loss function

$$L(A) = \frac{1}{2}\sum_{i=1}^{N} a_i |\mathbf{b}_i - A\mathbf{r}_i|^2 \tag{34}$$

Where N is the total number of body vectors, and a_i are non-negative weights. For two observations, i.e. $N = 2$, Wahba's problem is solved with the weights

$$a_i = \frac{c}{\sigma_i^2} \tag{35}$$

where $\sigma_i^2 = \sigma_{r_i}^2 + \sigma_{b_i}^2$ is the sum of the two measurement vector variances $\sigma_{r_i}^2$ and $\sigma_{b_i}^2$, and c is given by

$$c^{1/2} = \sigma_{tot} = \left(\sum_{i=1}^{N} \sigma_i^{-2}\right)^{-1/2} \tag{36}$$

so that the weights, a_1 and a_2, sum to unity.

Using these weights, the estimate of $A^{S/F}$ can be found trough equation (37), [6].

$$\hat{A}_{Wahba}^{S/F} = \frac{a_1}{\lambda}\left[\mathbf{b}_1\mathbf{r}_1^T + (\mathbf{b}_1 \times \mathbf{b}_\times)(\mathbf{r}_1 \times \mathbf{r}_\times)^T\right] + \frac{a_2}{\lambda}\left[\mathbf{b}_2\mathbf{r}_2^T + (\mathbf{b}_2 \times \mathbf{b}_\times)(\mathbf{r}_2 \times \mathbf{r}_\times)^T\right] + \mathbf{b}_\times \times \mathbf{r}_\times \tag{37}$$

[6] Grace Wahba posed this problem in 1965 in the article *A Least Squares Estimate of Satellite Attitude*, [6]

where

$$\lambda = \left(a_1^2 + a_2^2 + 2a_1a_2\left[(\mathbf{b}_1 \cdot \mathbf{b}_2)(\mathbf{r}_1 \cdot \mathbf{r}_2) + |\mathbf{b}_1 \times \mathbf{b}_2|\,|\mathbf{b}_1 \times \mathbf{b}_2|\,\right]\right)^{1/2} \tag{38}$$

3.3 Solving for the three Euler angles

From equation (29) it is clear to see, that the second Euler angle ϕ_2 of the 3-2-1 body axis rotation can be extracted as

$$\phi_2 = \sin^{-1}(-[A^{S/F}]_{13}) \tag{39}$$

If $\cos\phi_2 \neq 0$ the other two Euler angles can be determined by[7]

$$\phi_1 = \text{atan2}\left(\gamma[A^{S/F}]_{23}\,,\ \gamma[A^{S/F}]_{33}\right) \tag{40}$$

$$\phi_3 = \text{atan2}\left(\gamma[A^{S/F}]_{12}\,,\ \gamma[A^{S/F}]_{11}\right) \tag{41}$$

where $\gamma = \pm 1$ is the sign of $\cos\phi_2$ and atan2 is the arctangent function with two arguments[6].

[7] If $\cos\phi_2 = 0$ the attitude matrix becomes ill-defined. However, it is still possible to extract the Euler angles. In [6], chapter 2.9.6, the steps in this calculation is explained. It will not be expanded on in this thesis however, as it is a special case, and the issue was not encountered during data processing.

4 Experimental Set-up

To test the chosen sensors' ability to determine attitude, an experimental set-up capable of mimicking sun light, the magnetic field of the Earth and the rotational motion of a non-detumbled[8] spacecraft was needed. Also, an object acting as the spacecraft would be needed. Due to their limited size and simple geometry, a satellite mock-up of the same dimensions as a CubeSat[9] was chosen. In the following the set up used for testing, which can be seen on figure 9, will be examined.

4.1 The Overall Set-up

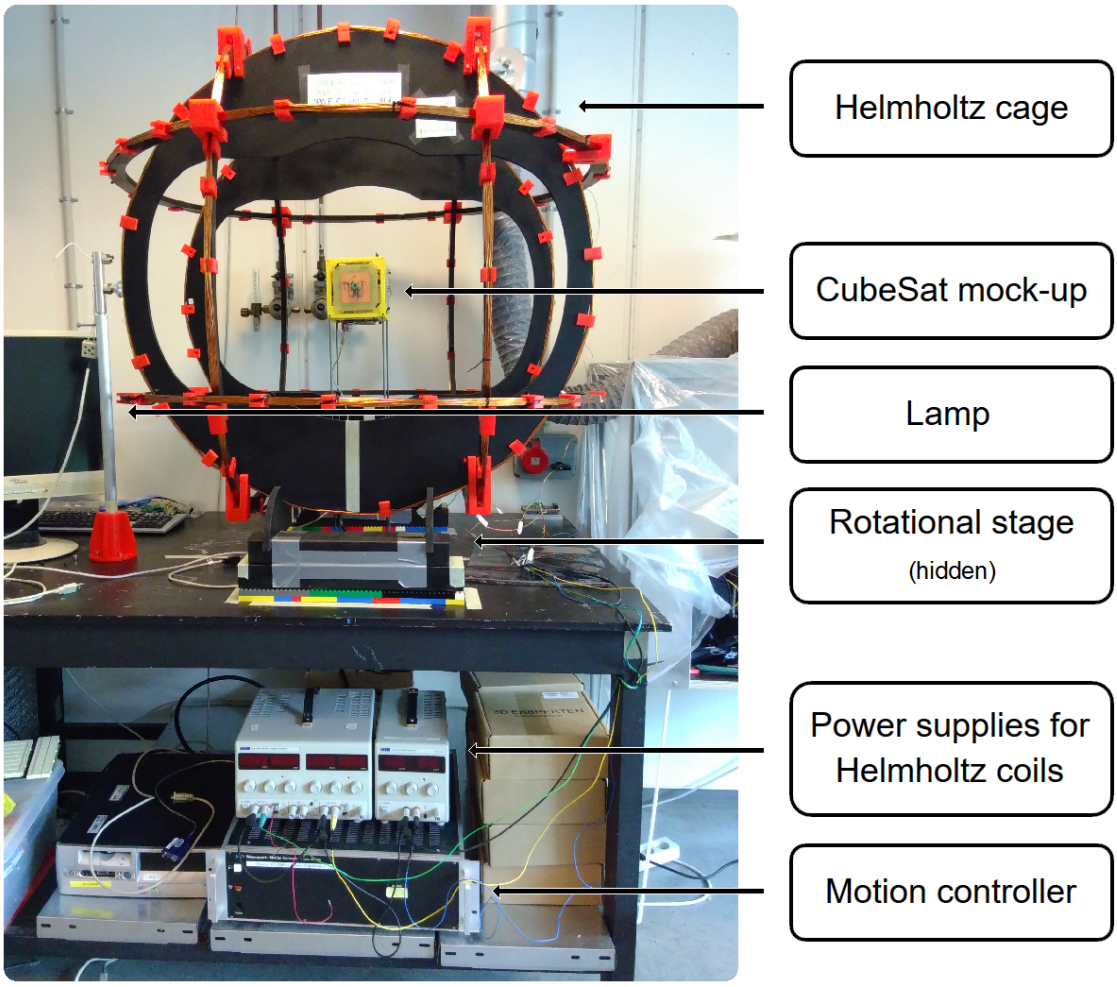

Figure 9: The full experimental set up.

The Helmholtz cage was build in a previous project. The two main purposes of the Helmholtz cage are to nullify the Earth's magnetic field, so characterisation and calibration of magnetic

[8]Detumbling refers to the act of stopping/slowing the rotation of a newly launched spacecraft, until the desired spin rate or orientation is acquired.

[9]The standard dimensions of a CubeSat (short for cubic satellite) are $100 \times 100 \times 100$ mm.

sensors can be performed, and to create a variable magnetic field for attitude determination tests. The current in the three coils is set by the three **power supplies** underneath the cage.

The CubeSat mock-up holds the sun and magnetic sensors, and will be thoroughly examined in section 4.2.

The lamp is an incandescent projector light bulb and is used to simulate the sun light.

The rotational stage, which is hidden by the Helmholtz cage stand on figure 9, holds the CubeSat mock-up and is capable of turning 350 deg in the horizontal plane. The rotational stage is controlled through **the motion controller**, placed underneath the Helmholtz cage. This specific model is a Newport MM3000 motion controller.

4.2 The CubeSat Mock-up

The CubeSat mock-up can be seen on figure 10. The cubic structure was 3D printed at DTU.

Figure 10: The CubeSat mock-up. Two of the sun sensor panels can be seen.

As will be fully described in section 5.2 a three-axis magnetometer (MAG3110) is used as a stand-in for the PHEBS. Therefore the current mock-up does not involve any PHEB sensors. The six sides of the cube were covered by three different types of panels. Four panels simply contained

a sun sensor as well as the electronics used for amplification and digital conversion. One panel had both a sun sensor and a MAG3110. An finally, the last panel included the electronics needed for data collection as well as a sun sensor. As a result, all six sides of the CubeSat mock-up should have a sun sensor. Unfortunately, due to time limittions, only four sun sensors ended up being ready for testing. As the rotational stage was only capable of rotating the mock-up around one axis at a time, the panels with sun sensors were placed around the CubeSat mock-up, so 360 deg coverage around one axis could be acquired.

4.2.1 The Electronics

The optimal circuit for amplifying the current generated by the photo diodes of the sun sensors were found in both [4] and [7] to be a transimpedance amplifier, see figure 11. As each sun sensor consists of four photo diodes, four amplifiers would be needed for each sun sensor, as well as four analogue-to-digital converters (ADC).

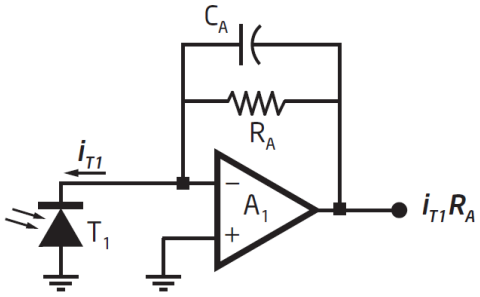

Figure 11: Transimpedance amplifier. Figure slightly edited from [7].

The data was collected on an Adafruit SD-card reader[10] connected to an Arduino pro mini[11]. The type of ADC used, a four input 16-bit ADC, ADS1115[12], only had four possible I^2C adresses, and as the CubeSat mock-up were to sustain six sun sensors, an eight channel I^2C bus switch, a TCA9548A,[13] was used.
The MAG3110 has internal ADC's, and therefore no additional ADC's were needed for this component.

[10] Adafruit SD-card: *https://www.adafruit.com/product/254*
[11] Arduino Pro Mini: *https://www.arduino.cc/en/Main/ArduinoBoardProMini*
[12] ADS1115: *http://www.ti.com/lit/ds/symlink/ads1115-q1.pdf*
[13] TCA9548A: *http://www.ti.com/lit/ds/symlink/tca9548a.pdf*

5 Characterisation of the Sensors

5.1 The Sun Sensors

The goal of the sun sensor characterisation is to find the linear relation described in section 2.1, see figure 4.
The CubeSat mock-up included four sun sensors. These will be referred to as SS1, SS2, SS3 and SS4 in the following. Each sun sensor consists of four photo diodes numbered 1 through 4. As an example, the current produced by photo diode 3 on sun sensor 1 would be $I_{SS1,3}$. Photo diode 1 and 2 make up the diode pair capable of measuring θ_x, and photo diode 3 and 4 make up the diode pair capable of measuring θ_y.

5.1.1 Procedure

Arranging the CubeSat mock-up so the sun sensor to be characterised was turned -90 deg away from the light source, the mock-up was then turned 180 degrees clockwise. Having measured the currents from one photo diode pair, the mock-up was rearranged as to have the second photo diode pair's sensitive axis be aligned with the motion, and the procedure was repeated.

5.1.2 Results

The results of the characterisation of photo diodes 1 and 2 from SS1 can be seen on figure 12.

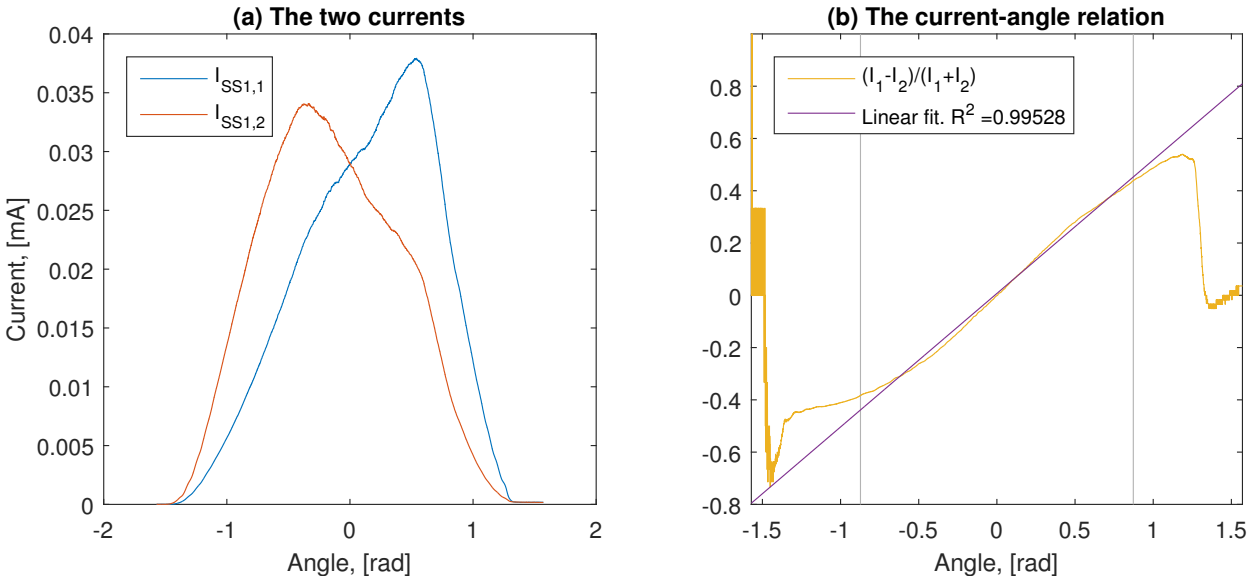

Figure 12: Results of the characterisation for photo diodes 1 and 2 of SS1.

Here the linear regression is based on $\theta \in [-50 : 50]$ deg, which is slightly less than the interval used in section 2.1.

While the chosen interval follows the linear regression quite closely, it is noted that the deviation from linearity is systematic. But whether this is inherent to the sun sensor, or due to the cone shaped light produced by the projector bulb is unknown.

The current-angle relation of this photo diode pair was found to be

$$\theta_x = 1.948 \text{ rad} \cdot \frac{I_1 - 1_2}{I_1 + 1_2} - 0.0138 \text{ rad} \tag{42}$$

Similar results were found for the remaining diodes, and their calibration graphs can be seen in appendix C.

5.2 Failure of the PHEBS

Previous works have shown, that the batch of PHEBS sensors used for testing in this project have very low normalized sensitivities and large biases, meaning that $V_y \neq 0$ when $B_y = 0$ [3]. Attemps to work around this bias and the low sensitivity have been carried out both in [3] and in this project. These attempts have however failed, and as such, the magnetic field sensor used for tests of the attitude determination algorithm will be a commercially bought three-axis magnetic sensor, MAG3110[14].
In the following an analysis of the sensitivity and the bias will be examined, and a hypothesis of why the batch has failed will be discussed.

5.2.1 Test circuit

Previous test circuits have focused on how to remove the bias and improve the sensitivity through analogue electronics, see [3]. This experimental setup was however designed to simply measure V_y - including its bias - and see how the PHEBS responds to changes in the magnetic field, without trying to enhance or alter the V_{y+} and V_{y-} signals in any way.
The schematic of this setup can be seen on figure 13.

[14] A datasheet for the MAG3110 can be found here: *http://www.nxp.com/assets/documents/data/en/data-sheets/MAG3110.pdf*

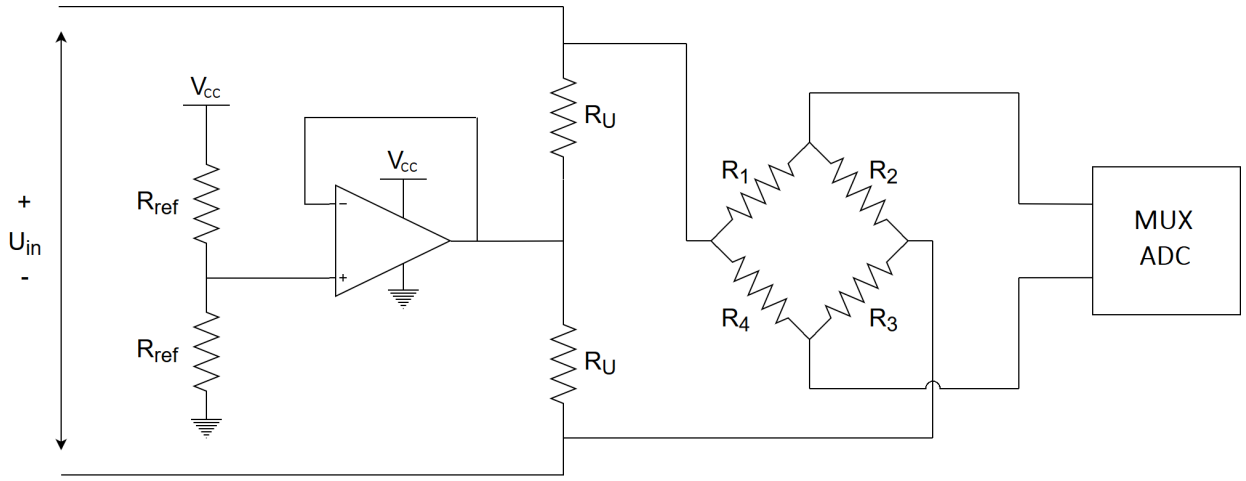

Figure 13: Schematic of the test circuit. Here V_{CC} = 3.3 V, R_{ref} = 1 kΩ, R_U = 10 kΩ, and the total resistance of the PHEBS, $R_{\text{PHEBS}} = (R_1 + R_2)||(R_4 + R_3)$ = 23 kΩ.

Here, U_{in} is set by a voltage generator, and could as such be varied. As stated by equation (6) the specific sensitivity should increase with U_{in}. Therefore the sensitivity, the bias and the signal-to-noise ratio of a single PHEBS are investigated for various values of U_{in}. The findings could be improved by repeating the measurements for several of the PHEBS, but the data and the results from this one experiment are however found to be sufficient in describing the shortcomings of this batch of PHEBS chips.

The circuit also involved the MAG3110 sensor for comparison. In the setup the PHEBS sensor was placed as to be sensitive in the y-direction of the MAG3110.
First the change in magnetic field was created by moving a strong magnet around the setup, simply to see if the y-signal from the MAG3110 and V_y from the PHEBS correlated.
Afterwards the change in magnetic field was generated by slowly turning the setup 360°. This would give a maximal and minimal value of V_y that would be in the same order of magnitude as the signals generated by a PHEBS in orbit.

5.2.2 Data processing

To illustrate the basic data processing, the data acquired from moving a magnet around the setup is used as an example. Figure 14 *(a)* and *(b)* show the raw data; the data from the MAG3110 and the signals V_{y+} and V_{y-} respectively. The large bias is clear on figure 14 *(b)*, and no clear correlation between V_y and the Y-axis of the MAG3110 is evident. Even when subtracting the bias, as has been done for figure 14 *(c)*, no correlation can be seen. Either, there simply is no signal generated from the PHEBS, or the signal is so small, that it disappears in noise. In an attempt to filter some of the high frequency noise, simple exponential smoothing is used.
First V_y is defined as in equation (43)

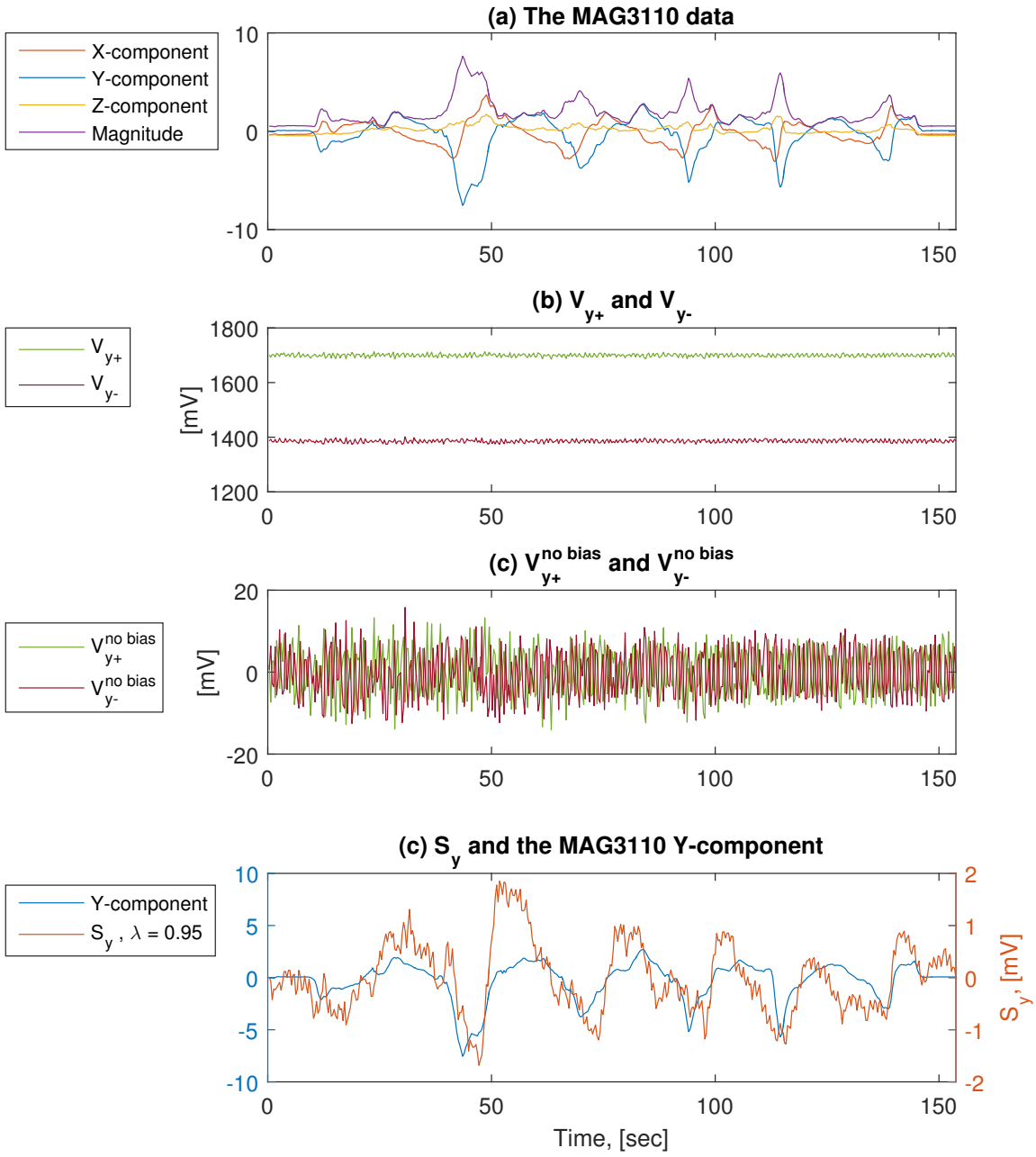

Figure 14: Steps in the data process. *Top, (a):* The signals from the MAG3110. *(b):* The unedited signals from the PHEBS sensor. *(c):* The signals from the PHEBS sensor, with the offset removed. *(d):* The exponentially smoothed V_y signal, S_y and the y-component from the MAG3110 for comparison. As can be seen from (*a*) and (*d*), the data output from the MAG3110 is treated as being unit less. The MAG3110 is not fully characterised, and as such the output is only proportional to the magnetic field components. But as all the magnetic vectors - both in the reference and body frame - are to be normalised, having an output simply proportional to the true magnetic field is sufficient.

$$V_y = V_{y+}^{\text{no bias}} - V_{y-}^{\text{no bias}} \tag{43}$$

V_y is now smoothed in accordance with the definition of simple exponential smoothing as given in [5];

$$S_{y,n} = (1-\lambda)V_{y,n} + \lambda S_{y,n-1} \qquad n = 0, 1, 2, .., N \tag{44}$$

where $\lambda \in [0, 1]$ and N is the total number of measurements. This means, that the smoothed value, $S_{y,n}$ is based $(1-\lambda)\cdot 100\%$ on the measured datapoint, $V_{y,n}$, and $\lambda \cdot 100\%$ on the previous smoothed point, S_{n-1}. As such, for high values of λ, high frequency changes can be smoothed off the data. Here, $\lambda = 0.95$ is used, and the resulting graph can be seen on figure 14 *(d)*.

Finally, correlation between the MAG3110 data and the PHEBS signals can be seen. It is however noted, that the PHEBS signals still are very noisy and of a very small amplitude < 2 mV. A similar data processing procedure was used for the remainder of the tests in treated in this section.

5.2.3 Results

The voltage applied to the PHEBS, U_{in} was set to the following values, $U_{in} =$ [10.0V, 12.5V, 15.0V, 20.0V, 22.5V, 25.0V, 27.5V, 30.0V]. For each increment in voltage, the circuit board was slowly rotated 360 degrees.
The first parameter to be investigated is the noise of the PHEBS signals.

2.3.3.1 Noise

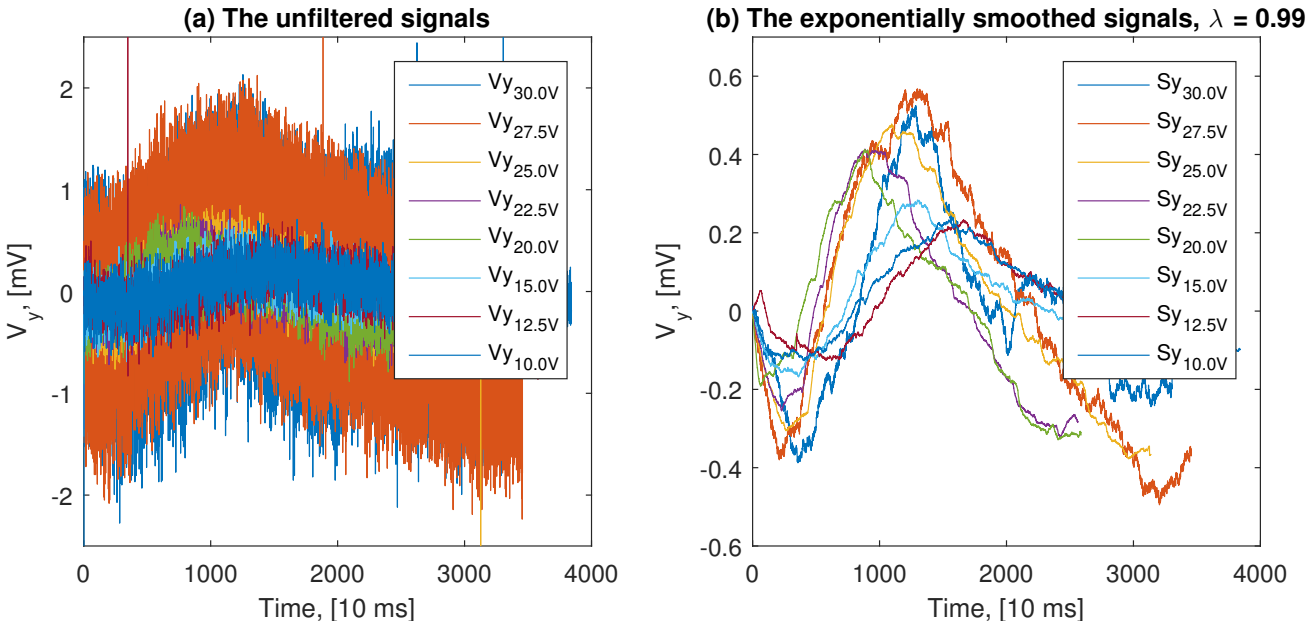

Figure 15: (*a*) The signals generated by the PHEBS for different values of U_{in}. Here the bias is removed as described in section 5.2.2. (*b*) The exponentially smoothed signals.

Figure 15 (*a*) and (*b*) show the unfiltered and the smoothed data. The difference between the two graphs is clear, and the noise is very evident. The signal to noise ratio (SNR) was calculated from the actual data and the smoothed data, and the SNR as a function of U_{in} can be seen on figure 16.

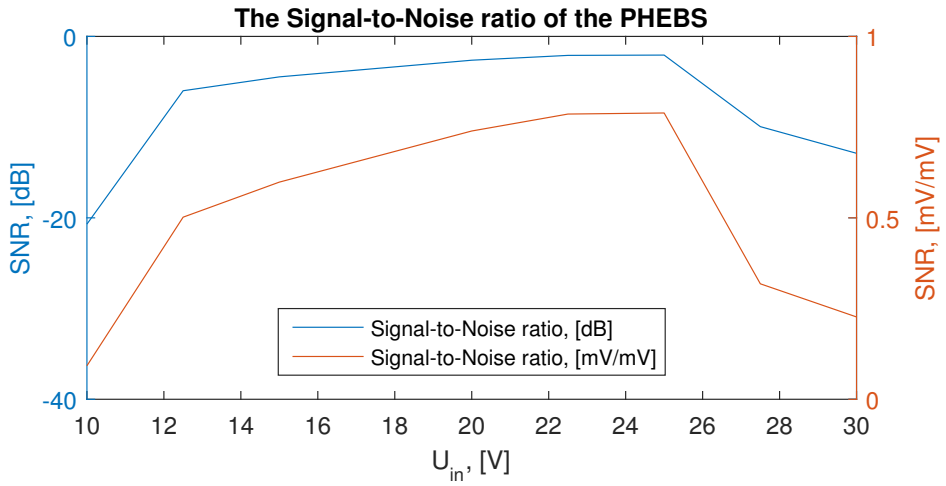

Figure 16: The signal to noise ratio of the PHEBS signals in both dB and magnitude.

As can be seen on figure 16, the usable signal is never larger than the noise, which renders the PHEBS practically useless. The SNR does increase with U_{in}, but the curve breaks at 25 V. Whether this is an inherent property of the PHEBS, or due to the circuit being build on a bread board (which are infamous for being noisy) is unknown. Either way, it seems improbable to overcome the issue of the SNR by simply increasing U_{in}, as - even before the 25 V break - the SNR seems to converge to a set value as the voltage increases.

2.3.3.2 Sensitivity and Bias

The sensitivity of the PHEBS should increase linearly with U_{in}, as stated in equation (6). As the PHEBS was rotated 360 degrees during this experiment, the sensitivity was calculated as

$$S = \frac{\Delta S_y}{\Delta B_y} = \frac{\max(S_y) - \min(S_y)}{2 \cdot \text{the horizontal intensity of Earth's magnetic field}} \tag{45}$$

The horizontal intensity of Earth's magnetic field was found through [12], and the output, as well as the date and coordinates used for calculations, can be seen in appendix B. The bias was calculated as the difference between the mean of V_{y+} and the mean of V_{y-} before any correction was applied. The trends can be seen on figure 17.

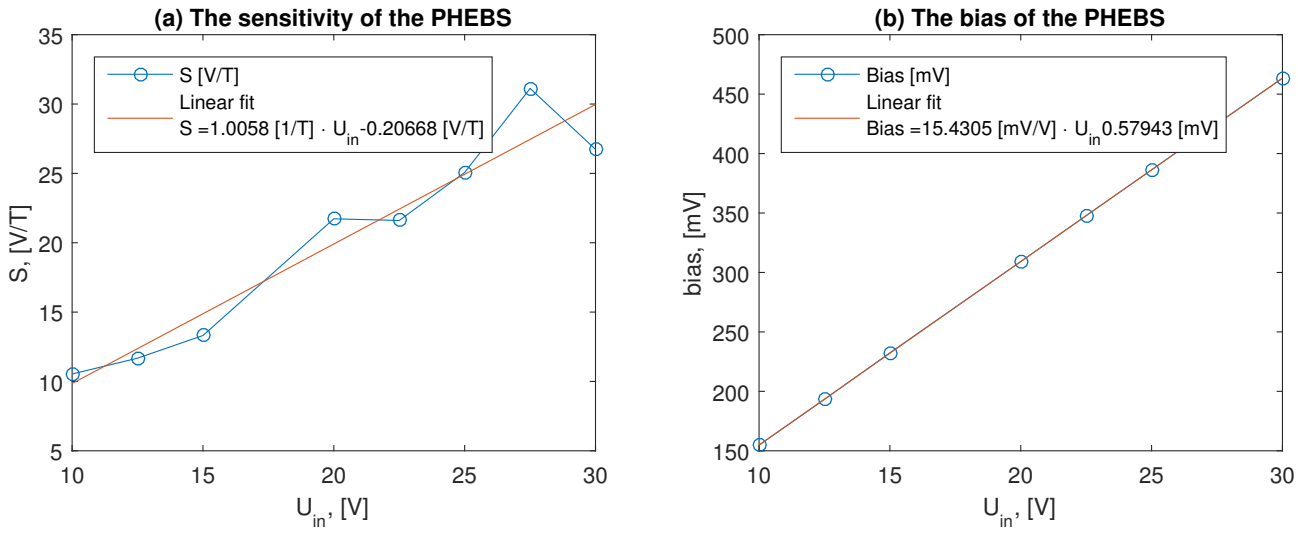

Figure 17: (*a*) The sensitivity of the PHEBS as a function of U_{in}. (*b*) The bias of the PHEBS as a function of U_{in}.

As expected the sensitivity appears to increase linearly as a function of U_{in}, as does the bias. The gain in sensitivity per voltage increase is however so small, that combined with the results of section 2.3.3.1 and the addition of the increase in the bias, the PHEBS chips initially chosen as the magnetic sensor for the project were deemed unfit.

5.2.4 Hypothesis of Why the PHEBS Failed

The tested batch of PHEBS chips were fabricated during the fall of 2016 [3]. Unfortunately, during the depositing of the magnetic metals, see figure 6 in section 2.2, the thickness of the AFM and FM layers were switched by mistake. As described in section 2.2, the AFM layer is used as a reference, forcing the magnitisation of the FM layer to line up with the easy axis when no outer field is present. The ratio of the AFM and FM layer thicknesses greatly influences the usability of the PHEBS. If the AFM layer is too thin, the sensor becomes uncertain, as the reference point will be ill defined. On the other hand, if the AFM layer is too thick, the sensor becomes insensitive, as a stronger outer magnetic field will be needed to change the magnitisation of the FM layer. Here, the later was the case.

The bias of the PHEBS sensor is likely due to non-uniformity of the resistance in the four meanders. Most PHEB sensors produced at DTU DanChip have few meander leads. These PHEBS have significantly smaller biases, but they're still present [1].

When increasing the number of leads - which should result in an increase in the normalised sensitivity, see equation (4) - the area where magnetic metal is to be deposited also increases. The large area of each PHEBS could allow for irregularities in the depositing to have a greater effect on the meander resistances than for a smaller sensor.

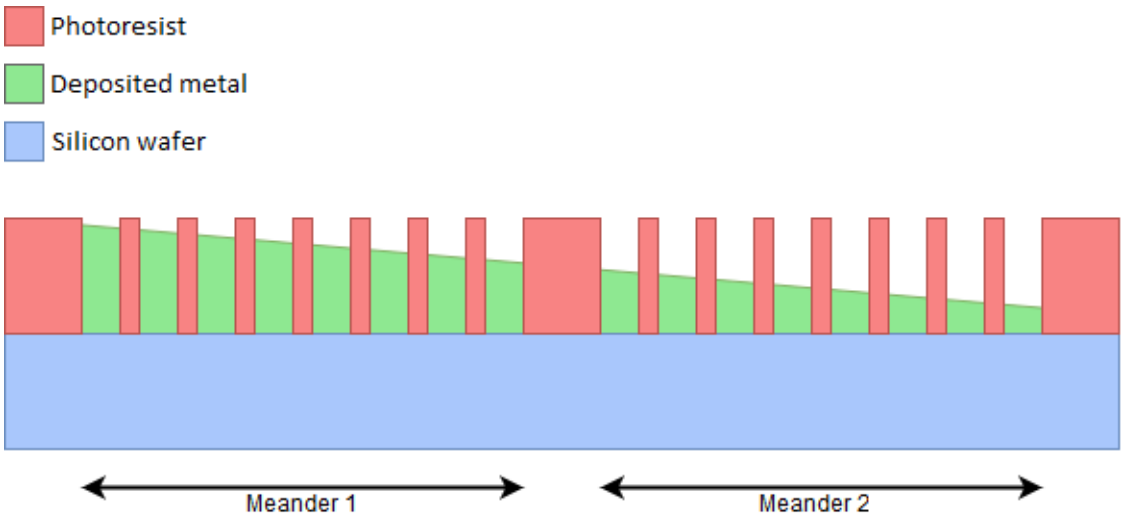

Figure 18: A cross section of a PHEBS sensor where lift-off of the resist is yet to be performed. The figure shows how uneven depositing of metals can result in a non-uniformity of the resistance in the meanders. The dimensions are greatly exaggerated.

As can be seen on figure 18 uneven depositing of metals could result in meander 2 having a higher resistance than meander 1, as meander 2's cross-section area is smaller. For a PHEBS with fewer meander leads, this difference would be less prominent.

Fabricating the PHEBS with the correct AFM and FM ratios would improve the sensitivity of the PHEBS. The uneven depositing could be due to human error in the alignment steps of the fabrication, resulting in varying widths of the meanders, or it could originate from an inherent unevenness in the machine used for depositing, thus creating non-uniform thicknesses of the meanders.

6 Calculating the Body Vectors From Sensor Data

6.1 Defining the Body and Reference Frame Vectors

To calculate the body vectors, first the reference and the body frame must be defined. Figure 19 show the orientation of both frames before rotation starts ($t = 0$).

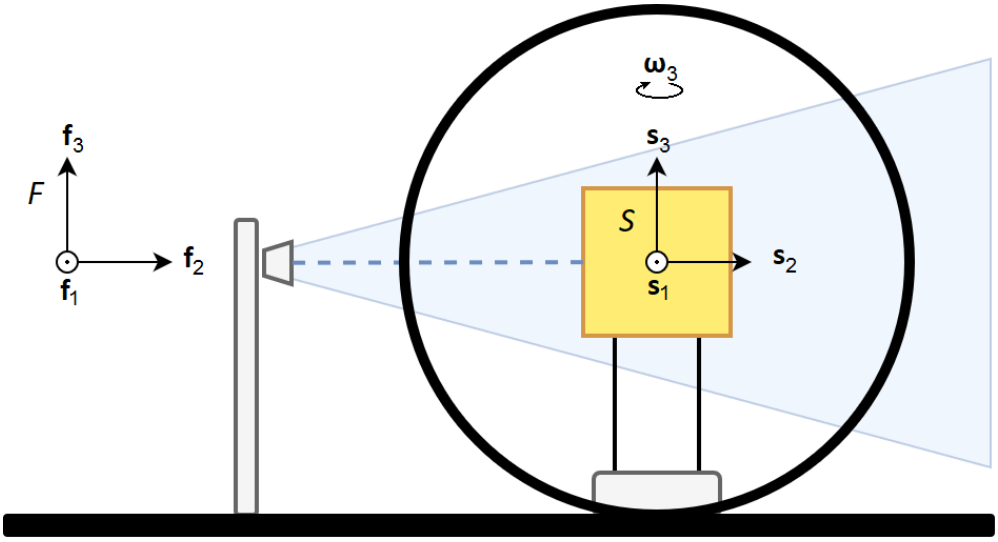

Figure 19: The two frames at time $t = 0$.

As can seen from figure 19 the two frames align at $t = 0$. As the reference frame is kept stationary, so are the reference vectors, $\mathbf{r}_1$ and. $\mathbf{r}_1$. Looking at figure 19 it is clear to see, that

$$\mathbf{r}_1 = [\ 0 \quad 1 \quad 0\ ]^T \tag{46}$$

This is however dependent on the light beams from the lamp being completely parallel with the second axis of F. The lamp does however produce cone shaped light, and this might reduce the accuracy of the reference vector and the data produced by the sun sensors.

The magnetic reference vector, $\mathbf{r}_2$ is found by measuring the magnetic field with the MAG3110 for a couple of minutes, while the CubeSat mock-up is stationary and the two frames are aligned. The individual components are then found by taking the mean of the MAG3110 output and normalising.

The data collected by the sensors are used to define the two vectors

$$\mathbf{B}_1 = [\ x_{Sun} \quad y_{Sun} \quad z_{Sun}\ ]^T \tag{47}$$

$$\mathbf{B}_2 = [\ B_x \quad B_y \quad B_z\ ]^T \tag{48}$$

where the three components are parallel with the three principal axes of the body frame, S. The body vectors are then defined as

$$\mathbf{b}_1 = \frac{\mathbf{B}_1}{||\mathbf{B}_1||} \quad (49) \qquad \mathbf{b}_2 = \frac{\mathbf{B}_2}{||\mathbf{B}_2||} \quad (50)$$

6.2 Calculating the body vectors

At $t = 0$, SS2 is in direct line of the light. Then as the mock-up rotates clockwise the order the panels are illuminated in is, from left to right

$$\text{SS2} \rightarrow \text{SS4} \rightarrow \text{SS3} \rightarrow \text{SS1} \rightarrow \text{SS2}$$

Figure 20 shows the unedited currents of all the photo diodes as the mock-up rotates as well as the data output from the MAG3110. The magnetic body vector, $\mathbf{b}_2$, is merely found by normalising the three magnetic components.

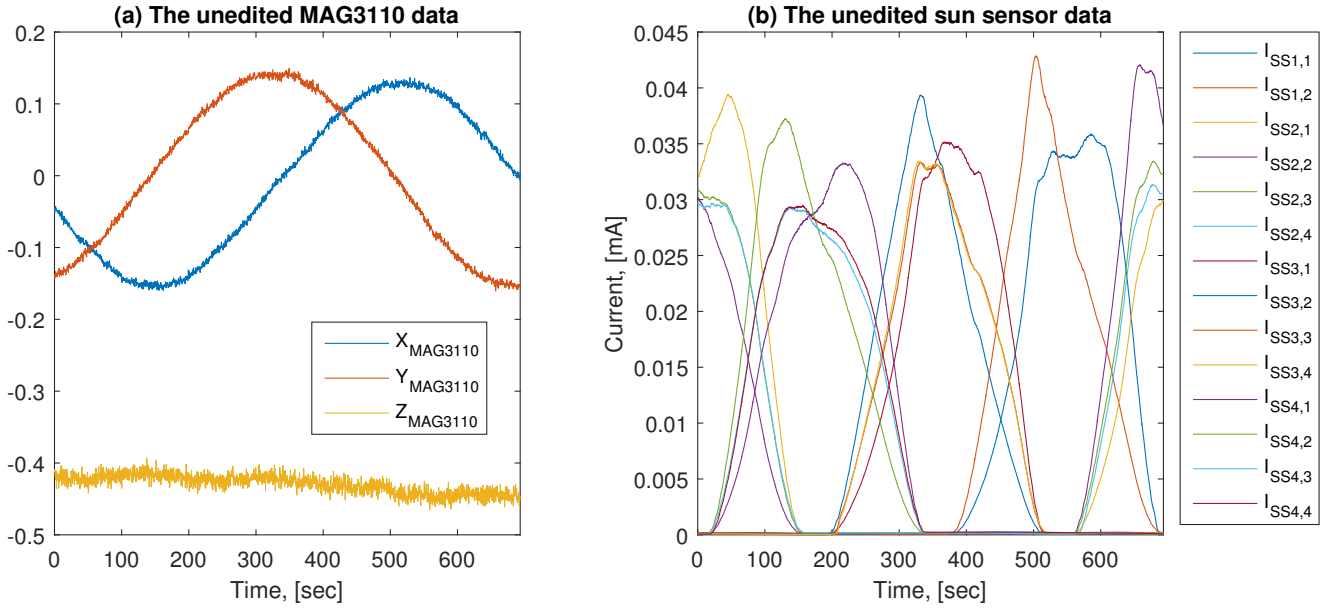

Figure 20: The unedited data the two body vectors, $\mathbf{b}_1$ and $\mathbf{b}_2$ will be calculated from. (*a*) shows the unedited MAG3110 data, and (*b*) shows the unedtited sun sensor data.

To find the solar body vector, $\mathbf{b}_1$, first the sun sensors' outputs were cropped to only include the data within the various sensors linear area, as described in section 5.1.2. This enables the angles to be found as a linear regression of the current ratios. It also insures, that the individual sun sensor's z-component is positive, and the definitions of equations (2) and (3) from section 2.1 can be used. The resulting normalised components can be seen on figure 21.

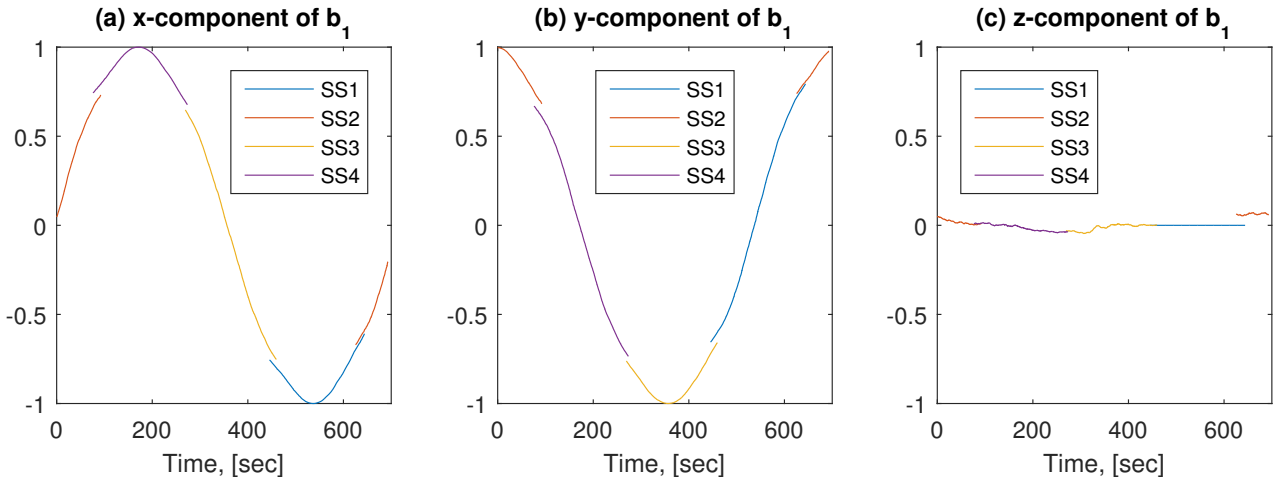

Figure 21: The three components of $\mathbf{b}_1$ as found by the different sun senors. Here the third component of SS1 is set to be 0, as photo diode 3 on SS1 did not work. As the mock-up only rotates around the horizontal plane, this component should be 0.

As can be seen from figure 21 the sensor output overlap. This means that $\mathbf{b}_1$ is defined throughout the rotation. In the areas of overlap, the final component values are simply found as the mean of the two component values. The final normalised body vectors can be seen on figure 22.

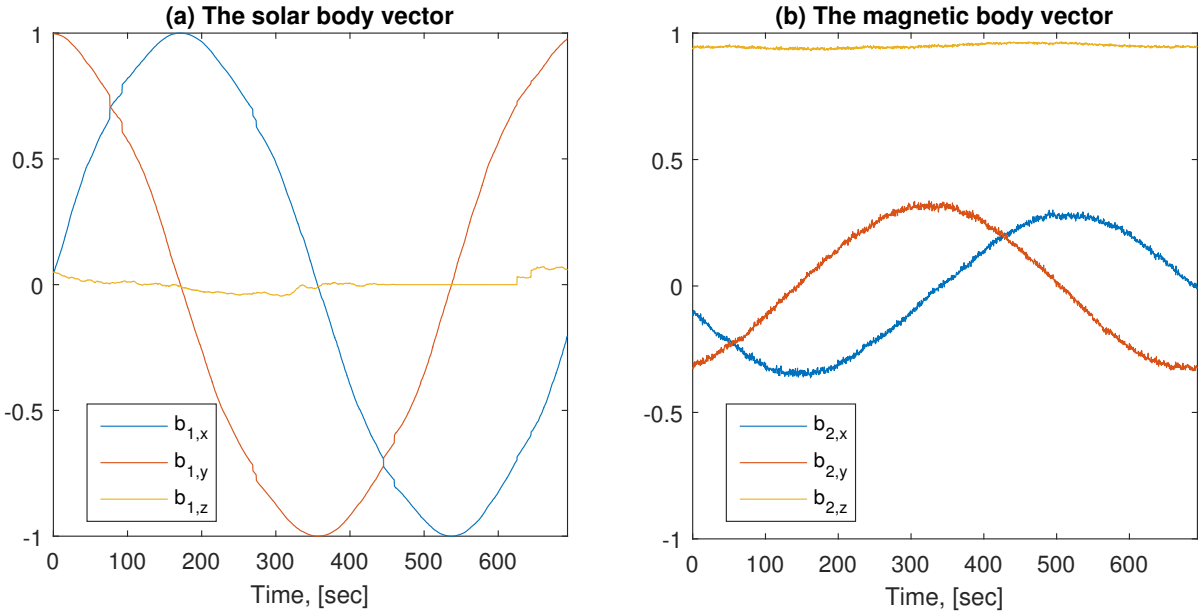

Figure 22: (*a*): The solar body vector, $\mathbf{b}_1$. (*b*): The magnetic body vector, $\mathbf{b}_2$. From (*a*) it is clearly seen, how the components have discontinuities in the areas of sensor overlap. The reason as to why the components, as seen on figure 21, do not align completely is either due to the linearisation being to rough of an approximation, or because the sensors aren't aligned perfectly on the CubeSat mock-up. Most likely it is a combination of the two.

Its these body vectors, and the previously defined reference vectors, that are used for the attitude determination in the following section.

7 Application of the Weighted TRIAD Algorithm

7.1 Determining the Variance of the Two Body Vectors

As described in section 3.2 the weights for the TRIAD algorithm are based on the variances of the reference and body vectors.

To find the body vector variances, $\sigma^2_{\mathbf{b}_1}$ and $\sigma^2_{\mathbf{b}_2}$, the sensors were set to measure the components for approximately 10 minutes while the mock-up was stationary. From these measurements the variances were calculated.

To determine whether the variance of the MAG3110 measurements were dependent on the magnitude of the field, the mock-up was turned 90 deg each 10 minutes. As such each of the three components would be of a different magnitude or each variance measurement. The results can be seen on figure 23.

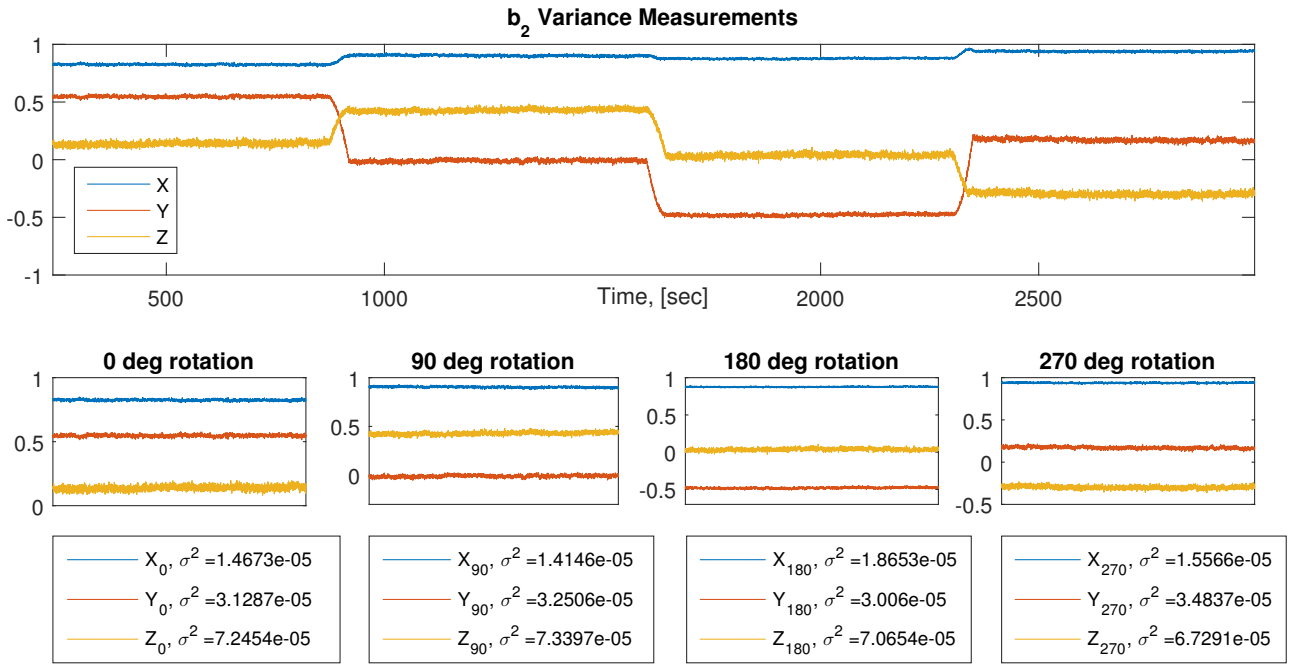

Figure 23: The magnetic variance measurements. *Top*: The entire measurements. *Bottom*: Each angle increment and the variances of the three components.

As can be seen from figure 23 the variance of each component remains within the same range

despite the angle and - and therefore also the magnitude. This means that the variance could be determined as a constant independent of the magnetude of the magnetic field.

The total vector variance, which must be a scalar, was found as the absolute sum of all the elements in the covariance matrix of the three components. This was done for each angle, and the highest variance was chosen;

$$\sigma^2_{\mathbf{b}_2} = 8.2945 \cdot 10^{-4} \tag{51}$$

A similar approach was used for the sun sensors, except the angles -45, 0 and 45 deg were used. The results can be seen on figure 24.

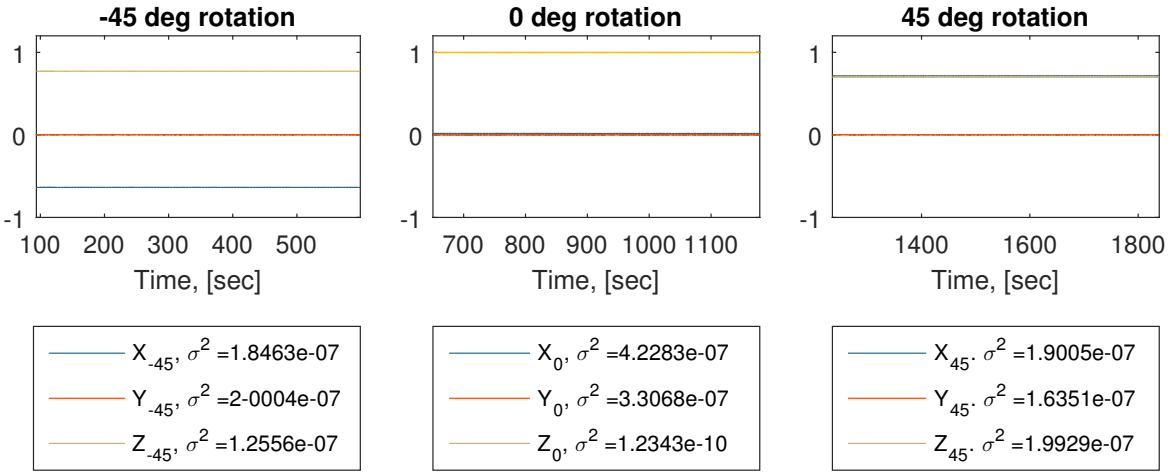

Figure 24: The sun vector variance measurements for three different indent angles.

It is noted that the variances of the sun vector components are very small by comparison. For 0 degrees, the z-axis component (the component parallel with the norm of the sun sensor surface) is extremely small compared to the z-component for the other two angles. This indicates, that the variance of the sun vector is not angle independent. However, when calculating the sum of the covariance matrices, all turned out to be of the same order of magnitude, $\approx 10^{-7}$. Therefore the total sun vector variance was set as a constant;

$$\sigma^2_{\mathbf{b}_1} = 7.9747 \cdot 10^{-7} \tag{52}$$

As $\mathbf{r}_2$, the magnetic reference vector, is found through the same magnetic sensor at $\mathbf{b}_2$, the variance of $\mathbf{r}_2$ was set equal to $\sigma_{\mathbf{b}_2}$.
The same was done for the reference sun vector, $\mathbf{r}_1$.

7.2 Application of Wahba's Problem for Two Observations

Following the equations from section 3.2 the attitude determination matrix for each measurement was found, and following the equations from section 3.3, the Euler angles were extracted. These angles, as well as the theoretical angles for comparison can be seen on figure 25.

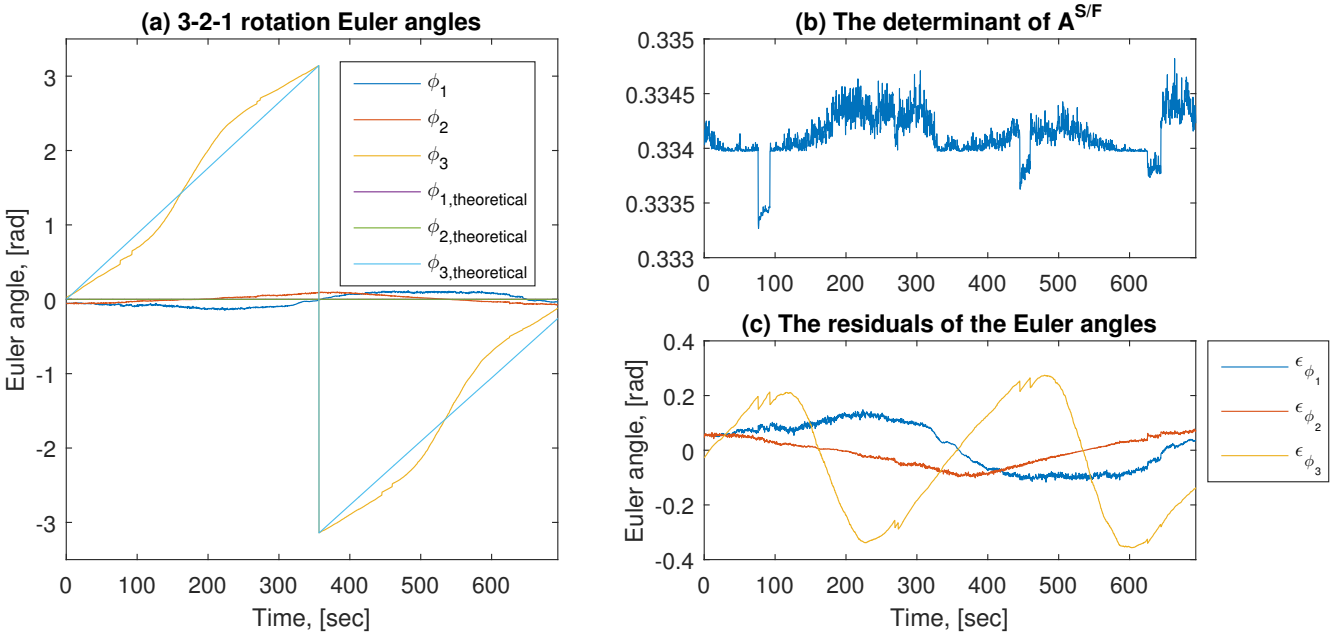

Figure 25: (*a*): The three measured Euler angles as a function of time, and the theoretical angles for comparison. (*b*): The determinant of each attitude matrix as a function of the time. It is noted, that the determinant is far from being +1 as it should. (*c*): The attitude error, calculated as $\epsilon_{\phi_i} = \phi_{i,theoretical} - \phi_i$ for $i = 1, 2, 3$.

From figure 25 (*a*) it is seen, that the three measured Euler angles follow the basic pattern of the theoretical angles. The attitude errors are however quite large, as can be seen from both 25 (*a*) and (*c*).

The cause of this is likely ill-defined attitude matrices. As figure 25 (*b*) shows, the determinant of $A^{S/F}$ is far from being +1. The attitude determination matrix should be based on two orthogonal triads. This would make $A^{S/F}$ orthogonal as well, and as with all orthogonal matrices, $\det(A^{S/F})$ should be ± 1. If $\det(A^{S/F}) \neq 1$, that would mean that the triads used were not orthogonal, resulting in faulty angle conversion.

As noted previously, the variance of the body sun vector was found to be significantly smaller that the variance of the body magnetic vector. But this variance was based on the measurements of a single sun sensor. $\mathbf{b}_1$ is however based on measurements from several sensors. As such, the value of $\sigma^2_{\mathbf{b}_1}$ is most likely too small, placing too much weight on the sun sensor measurements in the attitude determination process. Therefore the sun body vector weight is redefined.

7.3 Redefining the Weights

As discussed in section 3.2, Wahba's problem consists of finding the weights that minimise the loss function, equation (34). Here the weight, a_1 based on $\sigma^2_{\mathbf{r}_1}$ and $\sigma^2_{\mathbf{b}_1}$ will be redefined through a similar approach.

From figure 25 (*b*) it is clear, that the greatest attitude error is on ϕ_3. As the theoretical value of ϕ_3 is known, $\sigma^2_{\mathbf{b}_1}$ will be determined as the sun body vector variance that minimises the sum of squared errors (SSE) of ϕ_3:

$$\text{SSE} = \sum_{i=1}^{M} (\phi_{3,theoretical,i} - \phi_{3,i})^2 \tag{53}$$

Where M is the number of measurements.
This sum was calculated from various values of $\sigma_{\mathbf{b}_1}$, and the loss function graph can be seen on figure 26.

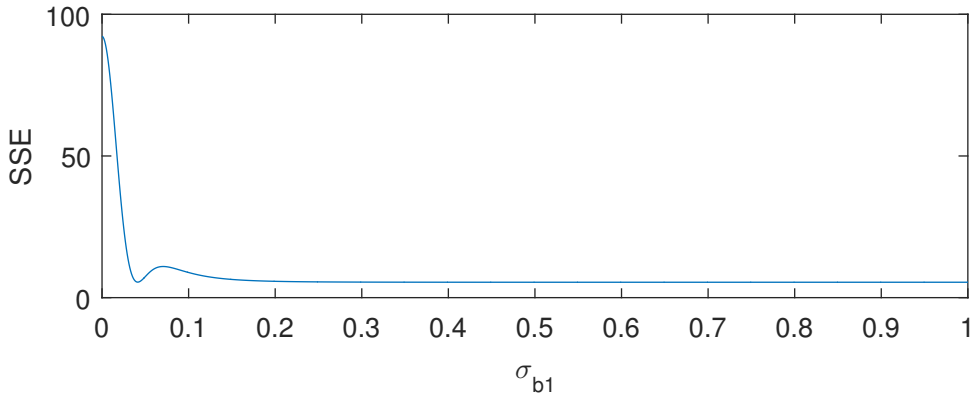

Figure 26: The sum of squared errors of the third Euler angle, ϕ_3, as a function of the solar body vector standard deviation, $\sigma_{\mathbf{b}_1}$

The minimum of this function was found for

$$\sigma_{\mathbf{b}_1} = 0.61462 \qquad \Rightarrow \qquad \sigma^2_{\mathbf{b}_1} = 0.37776 \tag{54}$$

This newly found value of $\sigma^2_{\mathbf{b}_1}$ was then used instead to set the weights.

7.4 Results

With the new weights, the results presented on figure 27 were obtained. From figure 27 (*a*) and (*c*) the improvement is clearly evident. Figure 27 (*b*) also shows how the determinant of the attitude determination matrices are much closer to +1 than previously.

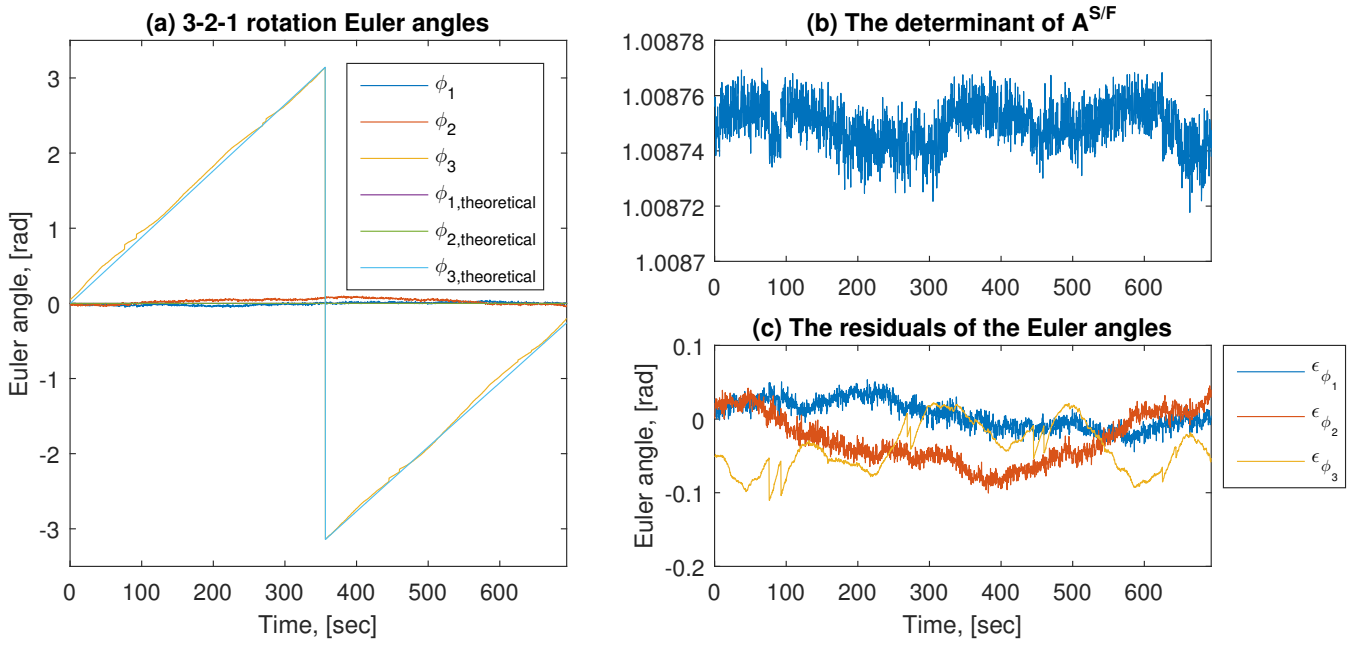

Figure 27: (*a*): The three measured Euler angles calculated with the new weights, and the theoretical angles for comparison. (*b*): The determinant of each attitude matrix as a function of the time. It is noted, that the determinant of $A^{S/F}$ is much closer to +1 now. (*c*): The attitude error, calculated as $\epsilon_{\phi_i} = \phi_{i,theoretical} - \phi_i$ for $i = 1, 2, 3$.

The maximum errors of each Euler angle, were found to be

$$\max \epsilon_{\phi_1} = 0.0534 \text{ rad} = 3.0596 \text{ deg} \tag{55}$$
$$\max \epsilon_{\phi_2} = 0.1005 \text{ rad} = 5.7582 \text{ deg} \tag{56}$$
$$\max \epsilon_{\phi_3} = 0.1105 \text{ rad} = 6.3312 \text{ deg} \tag{57}$$

8 Discussion

On figure 27 (*c*) it is noted, how both residuals for ϕ_1 and ϕ_2 do not resemble white noise, but instead seem follow slight sinusoidal motion. This could be due to the attitude determination being faulty, but it could also be a result of the experimental set up being slightly crooked. The wast majority of the experimental set up is assembled by hand, making it of limited accuracy. If the set up is crooked, the theoretical Euler angles will not describe the true motion of the CubeSat mock-up and this would result in faulty residuals. Therefore, instead of the sinusoidal shape of the residuals indicating erroneous attitude determination, it could be the an indication of the true, slightly crooked, rotation of the mock-up. This would make the determination of at least ϕ_1 and ϕ_2 more accurate than listed in section 7.4.

However, one of the main limitations of the experimental set up is its inability to adequately simulate tumbling motion. As of now, the rotational stage only allows for rotation around one axis, which is a very coarse approximation to the rotations a spacecraft would experience in orbit. From figure 27 (*c*) it is evident that the measurements of ϕ_3 are the most erroneous. This indicates, that the attitude determination is less accurate for axes that experience rotation. Therefore the maximum errors of ϕ_1 and ϕ_2 would most likely be larger than the ones listed in section 7.4 if rotation also occurred around the first and second axes.

The sun sensors are limited in that they are only usable within a certain angular interval. While it was shown in section 6.2 that the usable range of the sensors did overlap, resulting in a solar body vector defined for a full 360 deg rotation, it was also evident, that the components of $\mathbf{b}_1$ had discontinuities where sensor data overlapped. It was also shown in section 7.2 and 7.3, that the variance of $\mathbf{b}_1$ needed to be much larger than originally anticipated. This means, that despite full coverage, the body vector generated from the sun sensors was quite inaccurate.

A great deviation from the initial goals of this thesis was the exclusion of the PHEBS as a sensor. While proper fabrication most likely would result in more capable magnetic sensors, many of the challenges surrounding the usage of the PHEBS, as described in section 5.2, would still apply. Further research into the use of the PHEBS as a means attitude determination needs to be conducted before a final verdict on the PHEBS can be made.

9 Conclusion

In this Bachelor's thesis, the usage of the SunMag chip as a means of satellite attitude determination was explored.
An initial conclusion, was that the usability of the PHEBS used for this project was inadequate. Due to human errors in the fabrication, the sensitivity of the PHEBS was too low, and the inherent bias of the sensors made them unfit for attitude determination.
On the other hand, the sun sensors were capable of determining the solar body vector for a 360 deg rotation, and therefore usable for attitude determination. It was however found, that the solar

body vector was less accurate than originally anticipated. This initially resulted in the weighted TRIAD algorithm being unable to acceptably find the Euler angels. This issue was overcome by realising the inaccuracy of the solar body vector, and compensating by altering the weights used in the TRIAD calculations.
The uncertainties of the three Euler angles were found to be

$$\delta\epsilon_{\phi_1} = \pm 3.1 \text{ deg} \qquad \delta\epsilon_{\phi_2} = \pm 5.8 \text{ deg} \qquad \delta\epsilon_{\phi_3} = \pm 6.3 \text{ deg} \tag{58}$$

These uncertainties are however ambiguous as discussed in section 8.
While a complete attitude determination system utilising the SunMag chip was not completed, the work conducted and described in this thesis has made the initial progress towards this goal.

10 Future work

Carrying the project forward, the inclusion of all six sun sensors could would allow for solar body vector determination around other axis than the one explored in this thesis. The laboratory, where the practical work has been carried out, is in possession of an air-cushion driven spherical rotational stage. Altering the experimental set up to include this rotational stage would let the CubeSat mock-up rotate around all three axes.

As briefly mentioned in section 5.1.2 the sensitive area of the sun sensors was found to not be completely linear. Investigating the origin of this irregularity - whether inherent to the sensors or due to the limitations of the light source used for testing - could improve the sun sensors ability to determine the solar body vector.

While the PHEBS utilised in this thesis ended up not being included in the attitude determination system, properly fabricated PHEBS could be of future use. The fabrication of the full SunMag chip is scheduled to be undertaken during the summer of 2017. If the fabrication is successful, the SunMag could be tested in the experimental set-up constructed during the practical work of this thesis.

To increase the accuracy of the attitude determination, an extended Kalman filter could be implemented. Kalman filtering is often used in the context of attitude determination and control.

References

[1] Christensen et al. *Fabrication and Testing of Space Rated MEMS Based Sensor For Full AttitudeSolution - SunMag*. DTU space, 2016.

[2] Henriksen A. D. et al. *Planar Hall effect bridge magnetic field sensors*. Applied Physics Letters, 2010.

[3] Jensen, Alexander O. & Winther, Katcha. *Realization and characterisation of SunMag - A MEMS based attitude sensor for spacecrafts*. DTU Space, 2017.

[4] Larsen, et al. *Integration and qualification of MEMS based sun sensor*. DTU Space, 2008.

[5] Madsen, Henrik, *Time Series Analysis*. Chapman and Hall/CRC, 2007. ISBN 9781420059670

[6] Markley, F. Landis & John L. Crassidis, *Fundamentals of Spacecraft Attitude Determination and Control*, Springer, 2014, ISBN 9781493908011

[7] Rousing, Andreas W. *Space Grade Amplifier Electronics for MOEMS Sun Sensor*. DTU Space, 2014.

[8] Rousing, Andreas W. & Aslak, Ulf. *Ultrasensitive planar Hall effect bridge magnetic field sensors*. DTU Nanotech, 2013.

[9] Rousing, Andreas W. & Thiesson, Rikke. *MOEMS Sun Sensor for Attitude Control in Space with PHEBS Magnetometer & MEMS Thermistor*. DTU Space, 2014.

[10] Wie, Bong, *Space vehicle dynamics and control*, second edition. AIAA Education Series, 2008. Pages 323 - 347. ISBN 9781563479533

[11] https://earthobservatory.nasa.gov/Features/OrbitsCatalog/page2.php
Date: 07-06-2017

[12] https://www.ngdc.noaa.gov/geomag/magfield.shtml
Date: 01-05-2017

A Sun Sensor Dimensions

Parameter	Description	Value on used sun sensor
a	The height of a single triangular photo diode.	2400 μm
b	The half-width of the sun sensor.	750 μm
b'	The distance from the centre of the sun sensor to the centre of the illuminated area on the sensor.	–
d	The distance between the two triangular photo diodes.	N/A
c	The height of the slit.	2800 μm
s	The width of the slit.	550 μm
s'	The width of the illuminated area.	–
x_1	The centre height of the illuminated area on photo diode 1.	–
x_2	The centre height of the illuminated area on photo diode 2.	–
A_1	The illuminated area on photo diode 1.	–
A_2	The illuminated area on photo diode 2.	–
α	The smallest of the two acute angles of the triangular photo diode	32.0 deg
h	The height of the quartz layer.	495 μm
g	The height of the gold layer.	0.2 μm
u	The reduction of the width of the indent light beam due to the non-zero tickness of the gold cover.	–
θ_1	The indent angle of the sunlight.	–
θ_2	The angle of the refracted light.	–

Table 1: Description and values of the various measurements and parameters introduced on figure 3. When a parameter is dependent on the indent angle of the sunlight, its value is set to –.

B The horizontal intensity of the Earth's magnetic field

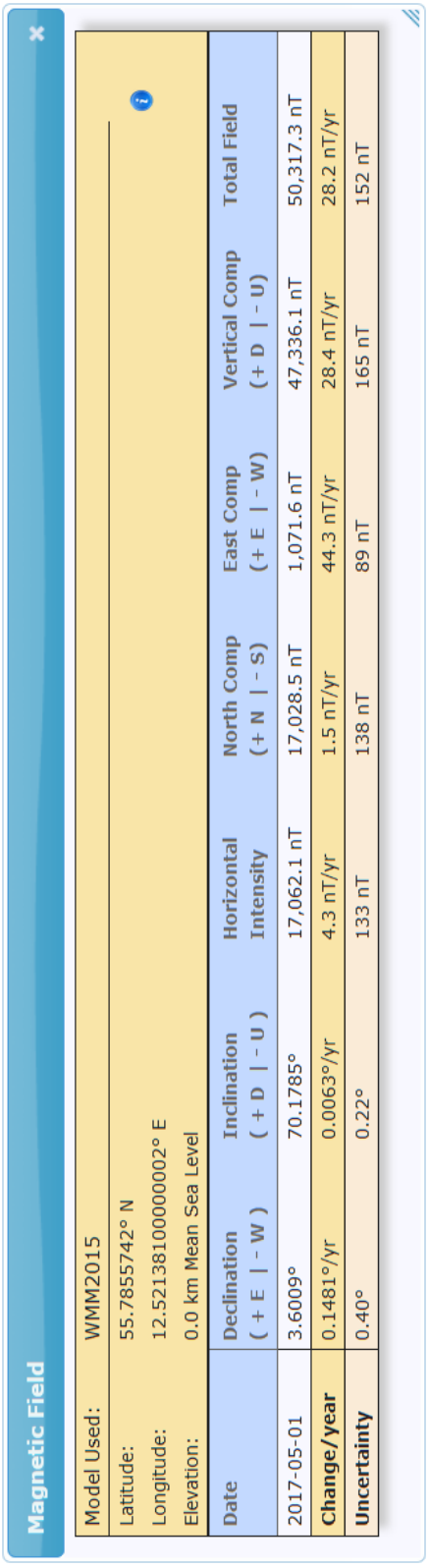

Magnetic Field

Model Used:	WMM2015
Latitude:	55.7855742° N
Longitude:	12.521381000000002° E
Elevation:	0.0 km Mean Sea Level

Date	Declination (+ E | - W)	Inclination (+ D | - U)	Horizontal Intensity	North Comp (+ N | - S)	East Comp (+ E | - W)	Vertical Comp (+ D | - U)	Total Field
2017-05-01	3.6009°	70.1785°	17,062.1 nT	17,028.5 nT	1,071.6 nT	47,336.1 nT	50,317.3 nT
Change/year	0.1481°/yr	0.0063°/yr	4.3 nT/yr	1.5 nT/yr	44.3 nT/yr	28.4 nT/yr	28.2 nT/yr
Uncertainty	0.40°	0.22°	133 nT	138 nT	89 nT	165 nT	152 nT

Figure 28: The data generated from [12]

C Sun Sensor Characterisation

SS2 x-axis

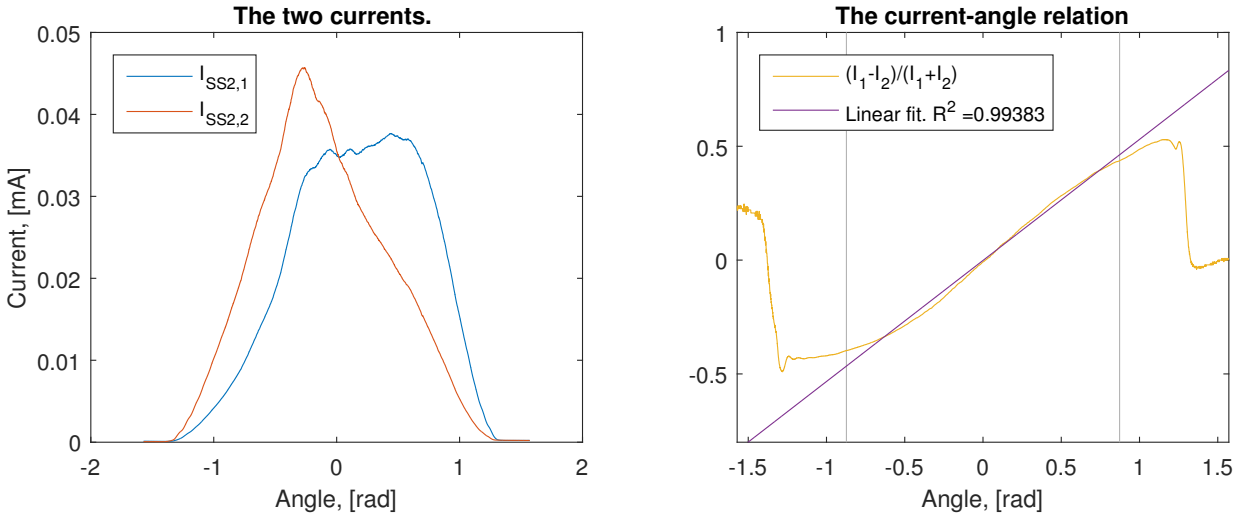

Figure 29: Results of the characterisation for photo diodes 1 and 2 of SS2.

$$\theta_x = 1.962 \text{ rad} \cdot \frac{I_1 - 1_2}{I_1 + 1_2} - 0.007226 \text{ rad}$$

SS2 y-axis

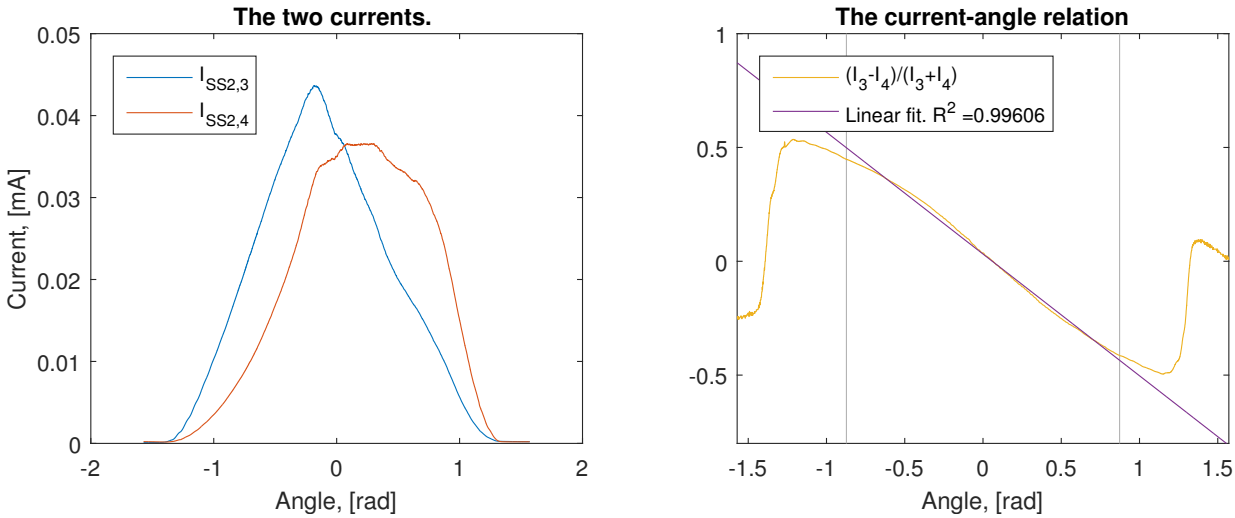

Figure 30: Results of the characterisation for photo diodes 3 and 4 of SS2.

$$\theta_y = -1.959 \text{ rad} \cdot \frac{I_3 - 1_4}{I_3 + 1_4} + 0.008882 \text{ rad}$$

SS3 x-axis

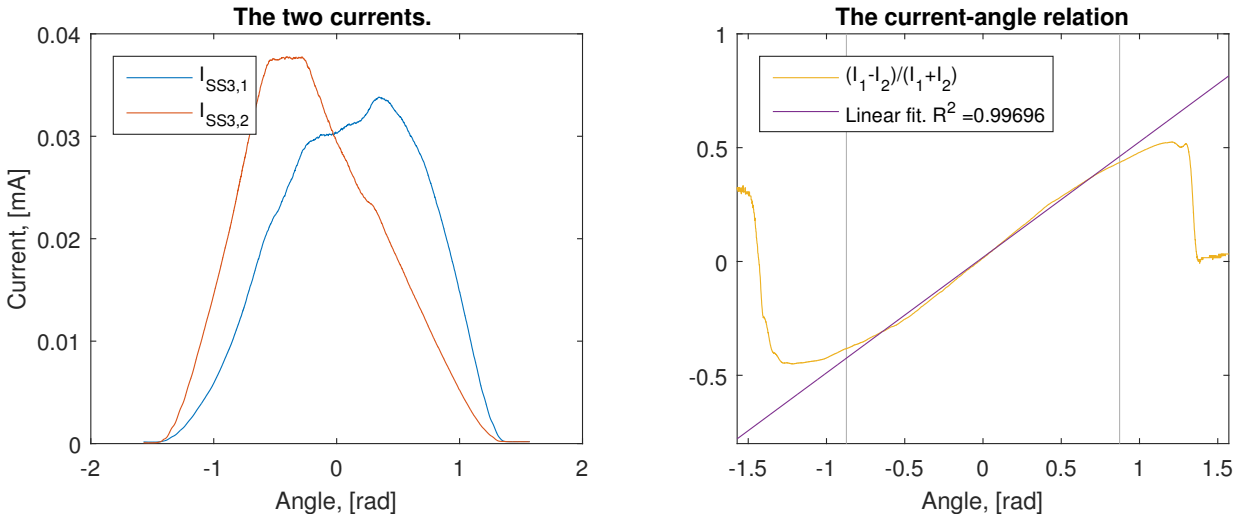

Figure 31: Results of the characterisation for photo diodes 1 and 2 of SS3.

$$\theta_x = 1.959 \text{ rad} \cdot \frac{I_1 - 1_2}{I_1 + 1_2} - 0.008456 \text{ rad}$$

SS3 y-axis

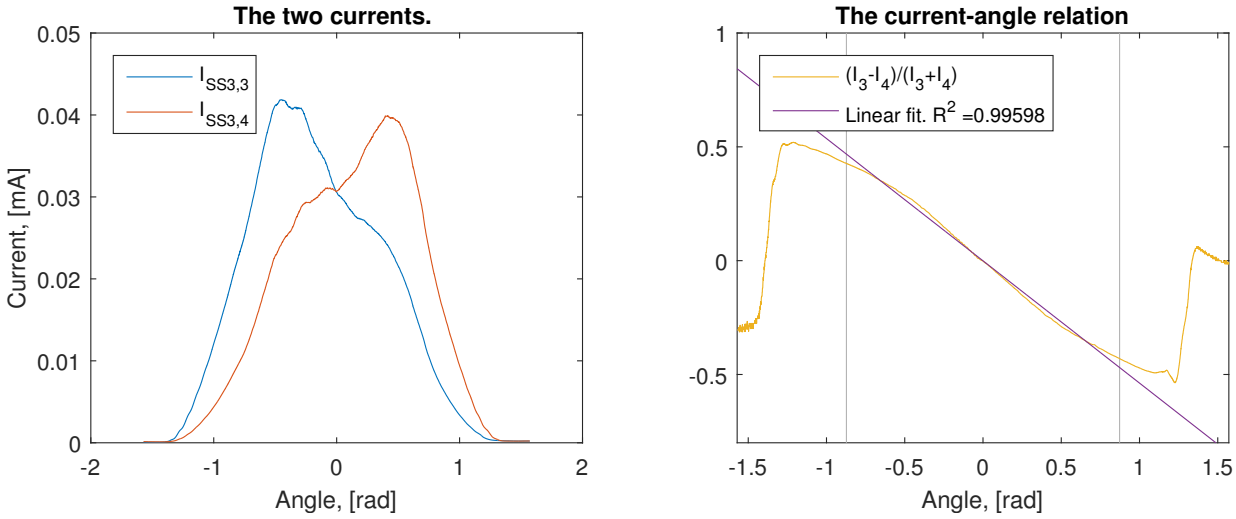

Figure 32: Results of the characterisation for photo diodes 3 and 4 of SS3.

$$\theta_y = -1.963 \text{ rad} \cdot \frac{I_3 - 1_4}{I_3 + 1_4} + 0.006834 \text{ rad}$$

SS4 x-axis

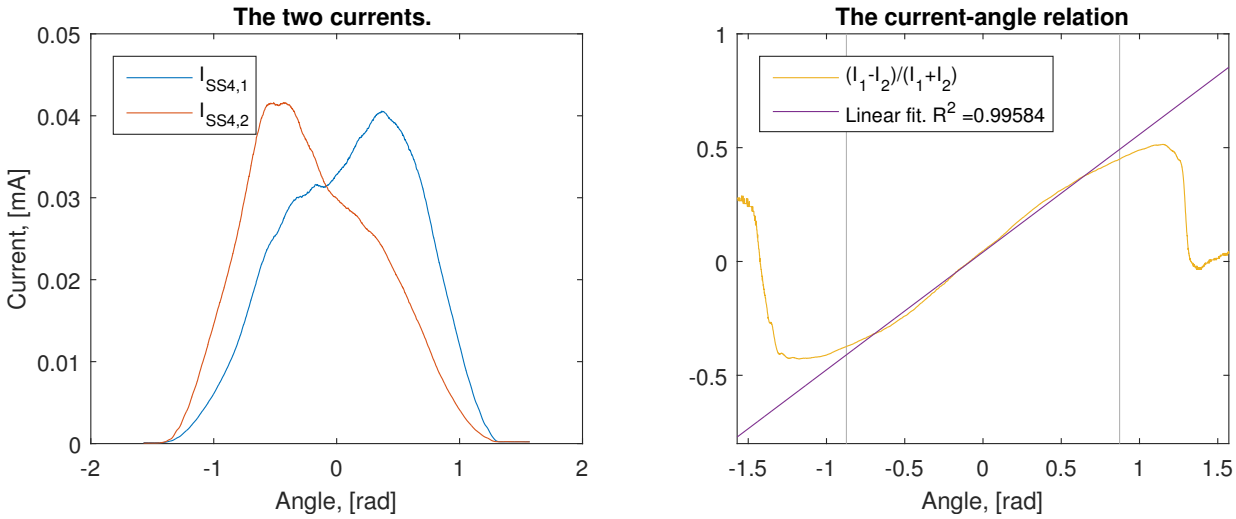

Figure 33: Results of the characterisation for photo diodes 1 and 2 of SS4.

$$\theta_x = 1.959 \text{ rad} \cdot \frac{I_1 - 1_2}{I_1 + 1_2} - 0.008882 \text{ rad}$$

SS4 y-axis

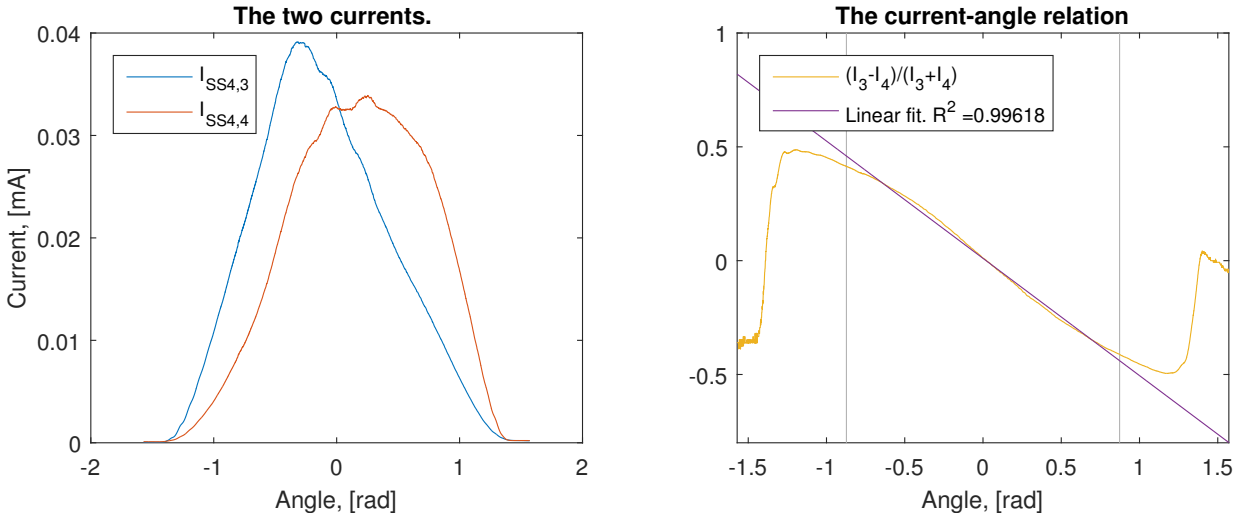

Figure 34: Results of the characterisation for photo diodes 3 and 4 of SS4.

$$\theta_y = -1.994 \text{ rad} \cdot \frac{I_3 - 1_4}{I_3 + 1_4} - 0.007779 \text{ rad}$$

DTU Space
National Space Institute
Technical University of Denmark

Elektrovej, building 327
DK - 2800 Kgs. Lyngby
Tel (+45) 4525 9500
Fax (+45) 4525 9575

www.space.dtu.dk